Chapter

Synthesis and Characterization of Multiferroic $BiFeO_3$ for Data Storage

Kuldeep Chand Verma

Abstract

Multiferroic $BiFeO_3$ deals with spintronic devices involved spin-charge processes and applicable in new non-volatile memory devices to store information for computing performance and the magnetic random access memories storage. Since multiferroic leads to the new generation memory devices for which the data can be written electrically and read magnetically. The main advantage of present study of multiferroic $BiFeO_3$ is that to observe magnetoelectric effects at room temperature. The nanostructural growth (for both size and shape) of $BiFeO_3$ may depend on the selection of appropriate synthesis route, reaction conditions and heating processes. In pure $BiFeO_3$, the ferroelectricity is induced by $6s^2$ lone-pair electrons of Bi^{3+} ions and the G-type antiferromagnetic ordering resulting from Fe^{3+} spins order of cycloidal (62-64 nm wavelength) occurred below Neel temperature, T_N = 640 K. The multiferroicity of $BiFeO_3$ is disappeared due to factors such as impurity phases, leakage current and low value of magnetization. Therefore, to overcome such factors to get multiferroic enhancement in $BiFeO_3$, there are different possible ways like changes dopant ions and their concentrations, $BiFeO_3$ composites as well as thin films especially multilayers.

Keywords: electric-driven magnetic switching, chemical synthesis, magnetoelectric, ferroelectric polarization

1. Introduction

Spintronic devices that electrically store non-volatile information are the potential candidates for high-performance, high-density memories due to their interdependence between magnetization and charge transport phenomenon. Since the capacitor stored information in the form of charges and the electric field moved these charges to transmit information. However, the magnetic recording is caused when the magnetic field used to read or write the information stored in the form of magnetization by measuring local orientation of spins. The behavior started to change in 1988, when the discovery of giant magnetoresistance provides a way for efficient control of charge transport through magnetization [1, 2], for example, the hard-disk recording. Hard disk drives (HDD) with a capacity of 10 MB were sold for ~$5300 in the 1980s, and were unaffordable for many during Apple and IBM PC era. However, HDDs with 16 TB capacity are available at the time of writing (2020). The computers in 1980s had memory of hundreds of kB that recently 8 GB random access memory (RAM). Even mobile gadgets have a dynamic random access memory (DRAM) capacity of ~4 GB, at the time of writing. This is possible by use of

charge property of the electron as well the spintronics devices make use of the spin property of an electron. Flash memory is an example, as it is a non-volatile memory as used in mobile applications [3]. However, the electrically induced bistable magnetization switching at room temperature - a necessary requirement for magnetic data storage - is the multiferroics [4]. The room-temperature manipulation of magnetization by an electric field using the multiferroic $BiFeO_3$ represents an essential step toward magnetoelectric (ME) control for spintronics devices [5].

1.1 Multiferroic memories for data storage

Multiferroic might hold the future for the ultimate memory device. The demonstration of a four-state resistive memory element in a tunnel junction with multiferroic barriers represents a major step in this direction [6–9]. For example, the thin films of lanthanum bismuth manganite remain ferromagnetic and ferroelectric down to thicknesses of 2 nm and, when used as a multiferroic tunneling junction, act as a four-state resistive system. Their spin-filter device as shown in **Figure 1(a)** is the tunnel junctions, which has tunnel barrier height is spin dependent because the bottom level of the conduction band in the ferromagnetic barrier is spin-split by exchange model. This allows the tunneling of electrons that to be efficiently filtered according to their spin. Gajek M *et al.* [10] suggested the large tunnel magnetoresistance in junctions that have a ferromagnetic electrode. The combination of these two effects - magnetoresistance plus electroresistance - yields a four-state resistive memory element. In comparison to the information stored in a capacitor, the resistive memories, on the other hand, can be read more simply, for example, by monitoring the source-drain current in a field-effect transistor. In order to make a multiple-state ME memory, one must be able to access the four states formed by electric polarization P and magnetization M, *i.e.* (+P, +M), (+P, −M), (−P, +M), and (−P, −M) [6].

1.2 Spin-transfer-torque magnetic random access memory

The spin-transfer-torque magnetic random access memory (STT-MRAM) devices stored information due to use of magnetic orientation in the ferromagnetic

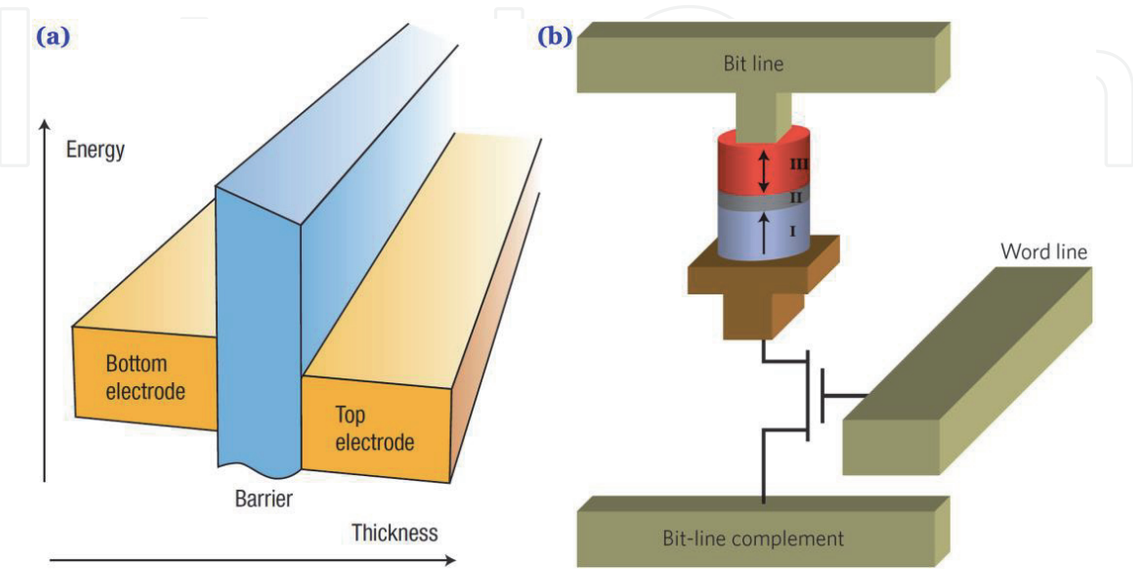

Figure 1.
(a) Tunnel junction (electrons tunnel from bottom electrode through barrier into top electrode): Schematic [6]. (b) Spin-transfer-torque magnetic random access memory (STT-MRAM) bit cell. A magnetic tunnel junction (I), a tunnel barrier (II) and a free-layer element (III), with both layers magnetized perpendicular to the plane of the junction (arrows). Bit is selected by a word line and transistor [7].

nanoparticles. For example, hard disk drives (use magnetic states to store information). In addition to hard disk drives, the STT-MRAM is a device that written and read electrically without any moving parts. The function of spin-transfer is to write information and such information is read by measuring the device resistance. The magnetoresistance plays role to measure percentage change in resistance between parallel and antiparallel magnetic spins of the electrodes of the magnetic tunnel junction. Such magnetic tunnel junction is made up by a ferromagnetic metal/insulator/ferromagnetic material [7]. **Figure 1(b)** shows a 1-bit STT-MRAM cell constituted by free layer and reference layer that are magnetized perpendicular to the plane of the junction [7]. The cell is constituted with a word line with a transistor that required for each cell. The biasing voltage could operate the cell with respect to bit lines and such read bias voltage measured the cell resistance to determine the bit state to be low of 100 mV. However, the write bias voltage is higher to allow the magnetic moment of the free layer taken to be reversed by using spin transfer torque.

1.3 Multiferroic $BiFeO_3$

The multiferroic $BiFeO_3$ (BFO) has high Curie temperature, $T_c \sim 1103$ K and Neel temperature, $T_N \sim 643$ K results into simultaneously ferroelectric and antiferromagnetic orders at room temperature. The ferroelectricity in BFO is originated by $6s^2$ lone pair electrons of Bi^{3+} via structural distortion, however, magnetism resulted with Fe-O-Fe superexchange interactions [11]. But the reported study pointed out BFO with low spontaneous polarization and saturation magnetization because superimposition of a spiral spins structure of BFO by antiferromagnetic order. In such spiral spin structure, the antiferromagnetic axis rotates BFO crystal with 62 nm long wavelength, which cancels out the macroscopic magnetization as well as affects ME coupling value. The superexchange between the octahedrally coordinated Fe^{3+} through the O ligand is responsible for the resulting antiferromagnetism. The presence of oxygen vacancies and the valence fluctuation (Fe^{2+}/Fe^{3+}) believed to be the main disadvantages causing large electrical leakage in BFO.

1.3.1 $BiFeO_3$ structure

The BFO structure is characterized with two distorted perovskite units connected by their body diagonal to build a rhombohedral unit cell as shown in **Figure 2(a)**. For such BFO structure, the two octahedral oxygen connected along (111) plane are rotated clockwise and counterclockwise at 13.8°. However, Fe ion is shifted 0.135 Å along same axis from oxygen that present at the octahedral position. The large displacement of Bi ions with respect to the FeO_6 responsible to induced ferroelectric polarization [12–14]. The spins in this BFO structure are incommensurate to form antiferromagnetic order. There is also some canting moments to give weak ferromagnetism due to Dzyaloshinskii-Moriya (DM) effect because the moments may oriented perpendicular to the (111) polarization direction to influence symmetry properties.

1.3.2 Lone-pair mechanism supporting multiferroicity

The spatial asymmetry that caused by anisotropic unbounded valence electrons around Bi^{3+} might to give lone pair mechanism (**Figure 2(b)**) responsible into room temperature ferroelectric polarization of BFO [12]. In $BiFeO_3$, a pair of Bi^{3+} valence electrons of the 6 *s* orbital not involved *sp* hybridization to generates a local dipole which resulting into ~100 μC cm^{-2} ferroelectric polarization below T_C = 1103 K. A long-range periodic antiferromagnetic structure arises below T_N = 643 K. The main

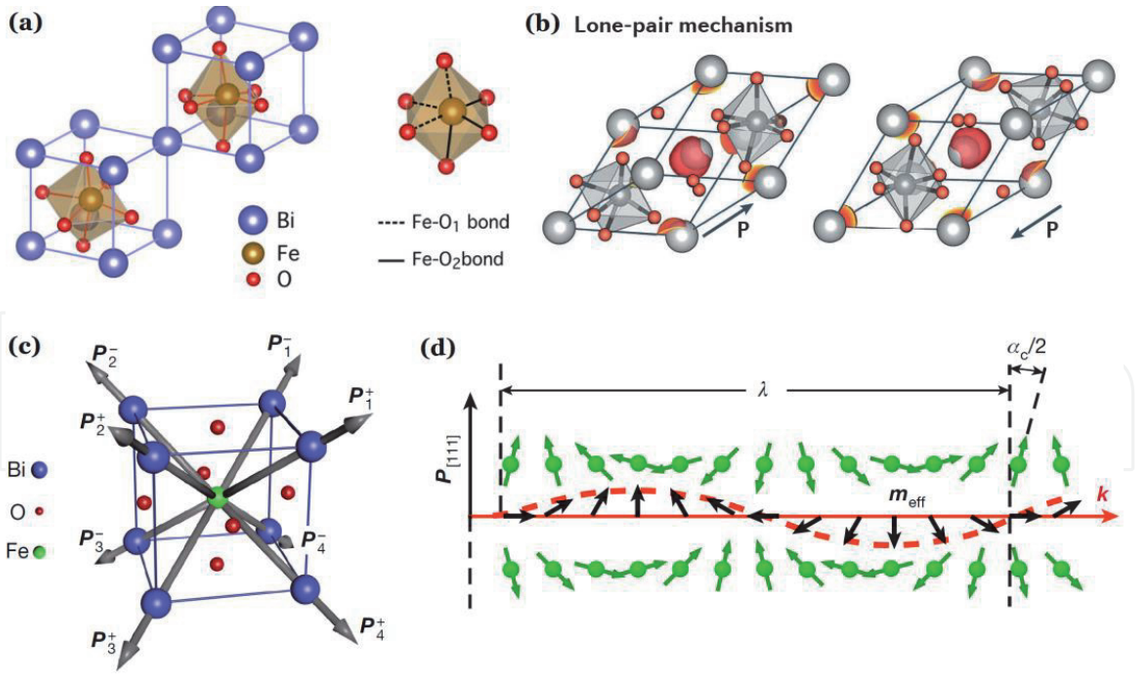

Figure 2.
(a) Rhombohedral (R3c) structure of $BiFeO_3$. (b) Ferroelectricity of $BiFeO_3$ due to lone-pair electrons (iso-surface: red) [12]. (c) Pseudocubic unit cell of $BiFeO_3$, (d) spin cycloid of canted antiferromagnetic alignments [13].

driving force of the ferroelectric phase transitions seems to be the stereochemical activity of the Bi 6 s lone-pair, resulting into a displacement of Bi and O sublattices. However, the Fe sublattice is also displaced and makes a sizeable contribution to the total electric polarization.

1.3.3 Ferroelectric and magnetic order in $BiFeO_3$

Bulk $BiFeO_3$ crystallized into a slightly distorted rhombohedral structure which commonly described by the pseudocubic unit cell (**Figure 2(c)**). The displacement of Bi ions relative to the FeO_6 octahedra gives rise to a strong ferroelectric polarization (100 μC cm^{-2}) along one of the [111] directions [13]. However, the magnetization in $BiFeO_3$ involved G-type antiferromagnet order with a cycloidal wavelength, $\lambda \sim 62$-64 nm was investigated by high-resolution neutron diffraction. As shown in **Figure 2(d)**, the normalized position of the spin cycloid propagation and the ferroelectric polarization vector might to induce ME coupling effect.

2. Synthesis of multiferroic $BiFeO_3$

The some synthesis methods used for $BiFeO_3$ are summarized in **Table 1**. Some of the listed methods are the derivatives of wet-chemical that deals with chemical reactions in the solution phase using precursors at proper stoichiometric conditions. Each wet-chemical synthesis route differs from the others in the sense that one cannot find a general rule for these kinds of synthesis approaches. Such wet synthesis schemes mostly used for fabrication of 2D nanomaterials. The wet-chemical processes offer a high degree of controllability and reproducibility of the 2D nanostructures. The solvothermal synthesis, template synthesis, self-assembly, oriented attachment, hot-injection, and interface-mediated synthesis are wet-chemical routes. However, the solvothermal and hydrothermal processes are mostly used to synthesize 2D nanostructures due to their simple and scalable steps.

Synthesis method	Reaction time	Precursor salts	Reaction condition	Shape control	Shape/size	Ref.
Wet chemical methods	Hours	Bi $(NO_3)_3.5H_2O$, $Fe(NO_3)_3$	HNO_3 used to adjust pH, Ethylene glycol & carboxylic acid are a polymerizing agent, annealed at 400°C/2 h	Good	13-70 nm particles	[15, 16]
Sol-gel method	Hours/ day	$Bi_5H_9N_4O_{22}$, $Fe(NO_3)_3$	Precursor concentration adjusted in 0.05-0.2 M using acetic acid & ethylene alcohol, annealed at 200-500°C	Good	10 nm particles	[17]
Co-precipitation method	Minutes	Fe $(NO_3)_3{\cdot}9H_2O$, Bi_2O_3	NaOH used as a precipitating agent, maintain pH 12, annealed at 400-600°C/1 h	Poor	200-250 nm particles	[18]
Hydrothermal process	Hours/ days	Bi $(NO_3)_3{\cdot}5H_2O$, $FeCl_3{\cdot}6H_2O$	Precursor salts dissolved in acetone, pH adjusted 10-11 by ammonia solution, Precursor solution transferred into teflon-lined steel autoclave and heated at 180°C for 72 h	Very good	45-200 nm diameter wires	[19]
Solution evaporation method	Hours	Fe $(NO_3)_3.9H_2O$, Bi $(NO_3)_3.5H_2O$, HNO_3	Tartaric acid and nitric acid used as precipitating and oxidizing agent, crystallization of the final powder take-place at 650°C/2 h	Good	22-31 nm particles	[20]
Microwave-assisted hydrothermal synthesis	Minutes	Bi $(NO_3)_3.5H_2O$, Fe $(NO_3)_3.9H_2O$	NaOH solution and polyethylene glycol were added to the precursors to obtain brown precipitates, solution irradiated by 300 W of MW irradiation for 30 min at 190°C with 2450 Hz	Good	20 nm diameter wires	[21, 22]
Self-catalyzed fast reaction process	Hours	α-Fe_2O_3, Bi_2O_3,	5 mol of tartaric acid ($C_4H_6O_6$) added to the precursors and heated at 250°C to begin to ignite and violently burn, final powder annealed at 650°C/2 h	Poor	100 nm particles	[23]
Conventional solid state	Hours/ days	Bi_2O_3, Fe_2O_3, Co_3O_4	Synthesis of $BiFeO_3$ powder from Bi_2O_3	Poor	100-200 nm particles	[24]

Synthesis method	Reaction time	Precursor salts	Reaction condition	Shape control	Shape/size	Ref.
reaction and thin film deposition of $BiFeO_3$-$CoFe_2O_4$			and Fe_2O_3 and heated at 800°C, $CoFe_2O_4$ powder prepared from Co_3O_4 and Fe_2O_3 using ball milling for 24 hours and heated at 1200°C/3 h, RF magnetron sputtering used for thin film deposition			
Chemical combustion method	Hours	$Bi(NO_3)_3$, $Fe(NO_3)_3$	Precursor solution mixed in polyethylene glycol, Urea added at 70°C and the combustion take-place, annealed at 600°C/5 h	Poor	50-500 nm nanostructures	[12]
Polymer-directed solvothermal	Hours	$Bi(NO_3)_3$.$5H_2O$, $Fe(NO_3)_3$.$9H_2O$	Precursor salt dissolved in HNO_3 and dipped by ethanol containing 1 g of PVP, and added 1.2 g of NaOH, transferred precursor solution into Teflon liner steel autoclave and heated at 180°C/6 h	Very good	1-D nanoparticles-assembled microrods	[25]
Sol-gel template process	Hours/ days	Bi $(NO_3)_3$.$5H_2O$, $Fe(NO_3)_3$. $9H_2O$	Porous nanochannel alumina (NCA) templates used, precursor salts mixed in nitric acid to get transparent, Citric acid & deionized water added, pH adjusted to be natural by using ammonia, urea added in 1/20th ratio, NCA templates added and heated at 80°C/20 h and annealed at 650° C/5 h	Very good	Nanotubes 150- 190 nm	[26]
Sonochemical technique	Hours	$Bi(NO_3)_3$.$5H_2O$, Fe $(NO_3)_3$.$9H_2O$, Mn $(OOCCH_3)_2$.$4H_2O$, Cr $(NO_3)_3$.$9H_2O$	In sonicated solution of Bi and Fe, add 5 ml of tetraethylene glycol and sonicated for 10 min, pH adjusted to 8 by adding ammonia and irradiated with a high intensity (100 W cm^{-2})	Good	Nanorods diameter 20-50 nm	[27]

Synthesis method	Reaction time	Precursor salts	Reaction condition	Shape control	Shape/size	Ref.
			ultrasonic radiation of 20 kHz, final product heated at 400°C/1 h			
Anodized alumina template technique	Hours	$Bi(NO_3)_3 \cdot 5H_2O$, $Fe(NO_3)_3 \cdot 9H_2O$	Precursor salts are mixed in 2-methoxyethanol, *p*H 4-5 by adding 2-methoxyethanol and nitric acid, anodized aluminum oxide template immersed in precursors for 12 h and heated at 750°C/12 h	Very good	Wires ~50 nm in diameter	[28]
Sol-gel based electrospinning	Hours	$Bi(NO_3)_3 .5H_2O$, $Fe(NO_3)_3 \cdot 9H_2O$	Precursors salts are neutralized with 2-methoxyethanol, pH 3-4 adjusted with Ethanolamine, Ethanol, glacial acetic acid, and poly vinyl pyrrolidone (PVP) added, solution was electrospun and the ultrafine fibers spun were collected in glass flake or Pt/Ti/SiO_2/Si substrate, final heating at 550° C/2 h	Very good	Nanofiber diameter in 100-300 nm	[29]

Table 1.
List the synthesis methods used to fabricate $BiFeO_3$.

3. Results and discussion

3.1 Structural analysis of $BiFeO_3$

3.1.1 X-ray diffraction of Pb substituted $BiFeO_3$

Figure 3(a) shows the X-ray diffraction (XRD) pattern of $Bi_{1-x}Pb_xFeO_3$ [x = 0 (BFO), 0.05 (BPFO5), 0.075 (BPFO75) and 0.1 (BPFO10)] nanostructures measured at room temperature [11]. All reflections are indexed to a rhombohedral structure of *R*3*c* space group. This is based on the character of the single (012) peak at around 22° and the splitting of the (104) and (110) peaks around 32°. The splitting of XRD peaks indicate the structural distortion due to tilting of FeO_6 octahedrons. The calculated lattice constants are a(Å) = 5.578, 5.577, 5.573 and 5.574 and c(Å) = 13.862, 13.893, 13.905 and 13.915, respectively for BFO, BPFO5, BPFO75 and BPFO10. The increase in lattice constant, c and decrease in a may be due to change in Fe-O bond lengths and Fe-O-Fe bond angles which have a significant effect on multiferroic properties.

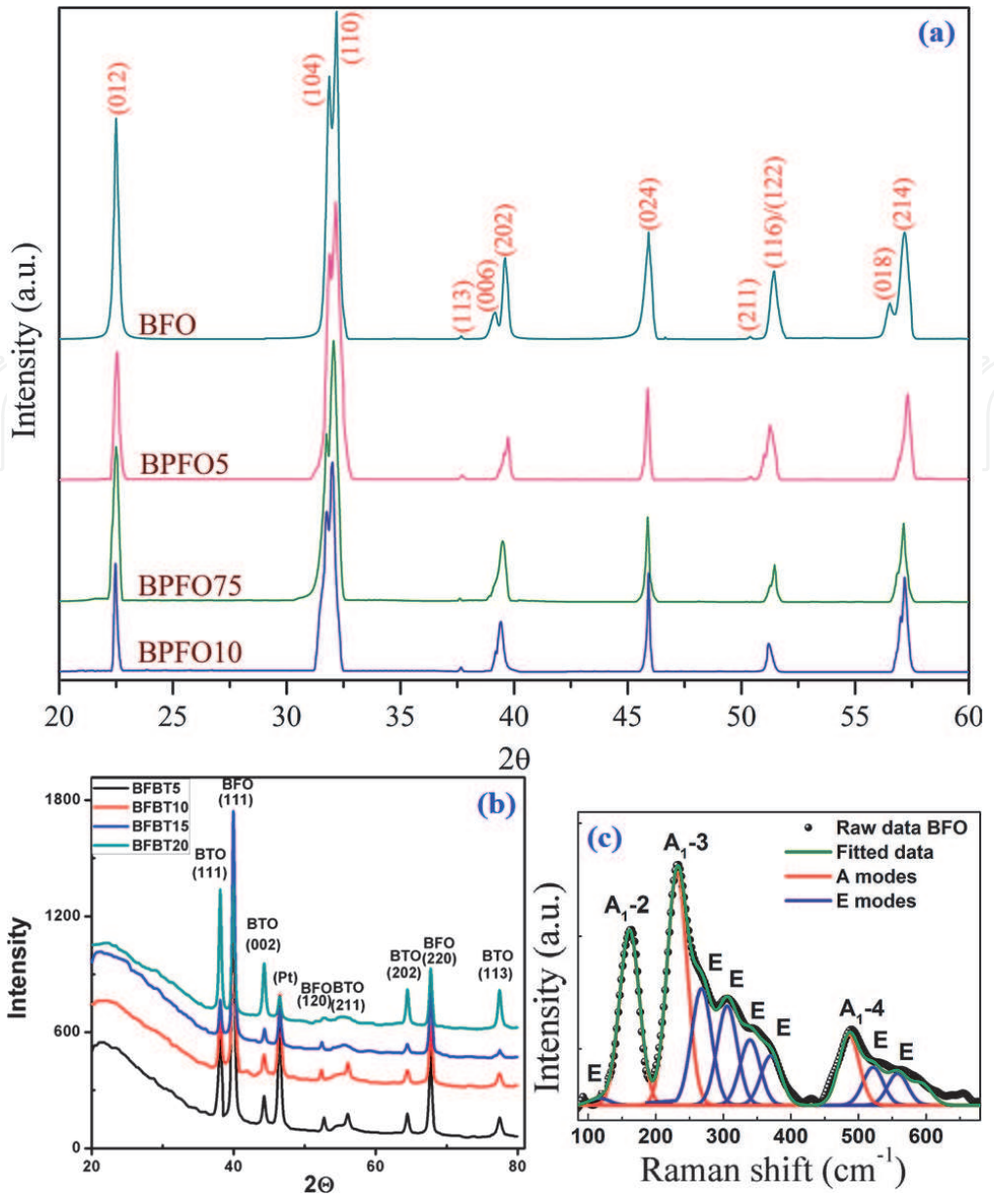

Figure 3.
(a) XRD pattern of $Bi_{1-x}Pb_xFeO_3$ multiferroic [11]. (b) Glancing angle X-ray diffraction (GAXRD) pattern of $BiFeO_3/BaTiO_3$ [thickness of BTO = 100 nm; while BFO = 50 nm (BFBT-5), 100 nm (BFBT-10), 150 nm (BFBT-15), and 200 nm (BFBT-20)] [30]. (c) Raman spectra of $BiFeO_3$ [31].

3.1.2 Crystalline structure of $BiFeO_3/BaTiO_3$ bilayer interface

Glancing angle XRD patterns, recorded at incident angle 1°, on different BFO/BTO bilayer thin films sputtered on $Pt/TiO_2/SiO_2/Si(100)$ substrates shown in **Figure 3(b)** [30]. Both BFO and BTO layers were found to be polycrystalline in nature without any impurity phase. The (110) plane of BFO appeared in θ-2θ mode only which was not be observed in GAXRD mode. It can be inferred that the bottom BTO layer promotes the formation of pure perovskite phase and high degree of (110) orientation in film texture.

3.1.3 Raman spectra of $BiFeO_3$ nanoparticles

The Raman spectrum of BFO obtained using 488 nm excitation wavelength depicted in **Figure 3(c)** [31]. The spectra have been deconvoluted into 10 individual components for BFO (3 A modes and 7 E modes). It was studied by DFT calculation of first principle that the low frequency Raman modes below 167 cm^{-1} are due to Bi atoms, and the modes between 152 and 262 cm^{-1} are due to Fe atoms [31].

However, oxygen atoms dominated with higher frequency modes above 262 cm^{-1}. The shifting and broadening of Raman modes with standard values suggests the presence of disorder and oxygen vacancies, and the internal microstrain due to Fe ions which might to change resulting magnetism.

3.2 Microstructural studies of $BiFeO_3$

3.2.1 FESEM image of $Bi_{0.9}Pb_{0.1}FeO_3$

Figure 4(a) shows the FESEM image of $Bi_{0.9}Pb_{0.1}FeO_3$ nanostructure [11]. The diameter of the nanorods, D = 125 ± 4 nm, and length, L = 900 ± 20 nm. However for pure BFO, the nanoparticles (D = 75 ± 2 nm) are formed [11]. This morphological variation with Pb doping into BFO is explained due to variation in the valence states of Fe ions due to oxygen vacancies. The substitution of Pb^{2+} into Bi^{3+} ions induces Fe^{2+}/Fe^{3+} ions in the BFO matrix that can influence lattice defects (oxygen vacancies) in the rhombohedral BFO phase. It results into an anisotropic growth along the *c*-axis.

3.2.2 $BiFeO_3$-$CoFe_2O_4$ self-assembled nanocomposite

Figure 4(b) shows a top-view SEM image of a square array with period 83 nm [32]. The bright rectangular islands visible in this image correspond to (111)-faceted tops of the $CoFe_2O_4$ pillars, while the darker area corresponds to single crystal

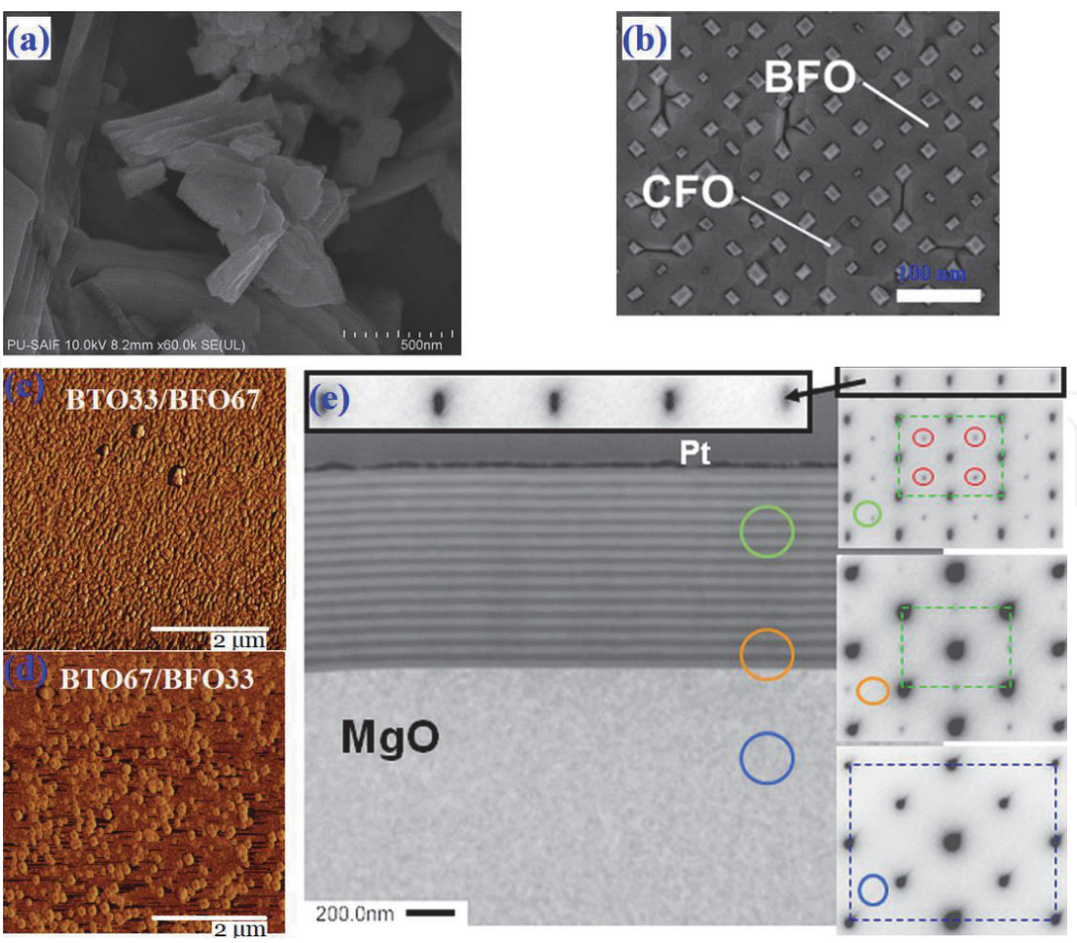

Figure 4.
(a) FESEM image of $Bi_{0.9}Pb_{0.1}FeO_3$ [11]. (b) Top-view SEM image of BFO-CFO nanocomposite [32]. (c and d) AFM surface images of BTO33/BFO67 and BTO67/BFO33 [33]. (e) STEM dark-field image of ($BaTiO_3$-$BiFeO_3$) × 15 grown on MgO [34].

$BiFeO_3$ matrix. This BFO-CFO nanocomposite was grown by pulsed laser deposition. The film thickness was between 50 and 100 nm.

3.2.3 Atomic force microscopy images of BTO/BFO thin films

The $BiFeO_3$ and $BaTiO_3$ were used to grow homogeneous composite thin films and multilayer heterostructures with 15 double layers by pulsed laser deposition [33]. The thin films are composites grown directly from mixed PLD targets with 67 wt% BTO/33 wt% BFO (BTO67/BFO33) and 33 wt% BTO/67 wt% BFO (BTO33/BFO67), respectively. **Figure 4(c)** and **(d)** are the AFM surface images of these two different composite films and the nanoparticle sizes are in the ranges 40-100 nm and 100-200 nm, respectively.

3.2.4 Scanning transmission electron microscopy (STEM) of $BaTiO_3$-$BiFeO_3$

Multiferroic ($BaTiO_3$-$BiFeO_3$) × 15 multilayer heterostructures show high ME coefficients, α_{ME} up to 24 V cm^{-1} Oe^{-1} at 300 K [34]. The STEM and SAED mapping results of the ($BaTiO_3$-$BiFeO_3$) × 15 multilayer are depicted in **Figure 4(e)**. The STEM cross section is shown 15 double layers $BaTiO_3$-$BiFeO_3$ at smooth interfaces. The octahedral tilt involves both clockwise and counter clockwise rotations around [111], which is parallel to ferroelectric dipole displacements to *R3m* phase. The difference between the lattice parameters of the tetragonal $BaTiO_3$ and rhombohedral $BiFeO_3$ layers can be detected by reflection splitting along the growth direction (inset in **Figure 4(e)** top).

3.3 Ferroelectric behavior of $BiFeO_3$

The $BiFeO_3$ is a rhombohedrally distorted perovskite material, which means that the ferroelectric polarization can have orientation along the four pseudo-cubic diagonals (<111>) [35–38]. The largest relative displacements are those of Bi relative to O, consistent with a stereochemically active Bi lone pair that might to induce ferroelectricity of $BiFeO_3$.

3.3.1 Ferroelectric polarization of Pb doped $BiFeO_3$ nanoparticles

The ferroelectric polarization of multiferroic $Bi_{1-x}Pb_xFeO_3$ nanostructures is given in **Table 2** [11]. In BFO, the lone-pair orbital of Bi^{3+} ($6s^2$) is stereochemically active and responsible for ferroelectric distortion. Here, the distortion is induced by Pb doping and therefore, by tuning the lone-pair activity. Generally, the ferroelectric behavior is weakened due to an increase in oxygen vacancies that form more

Sample	P_s ($\mu C\ cm^{-2}$)	P_r ($\mu C\ cm^{-2}$)	E_c ($kV\ cm^{-2}$)	J ($\mu A\ cm^{-2}$)	ε		MC (%)		T_{FE} (K)
					1 kHz	1 MHz	1 kHz	1 MHz	
BFO	0.75	0.35	7.66	10.31	6.2	5.1	0.68	0.61	644
BPFO5	1.76	0.63	6.03	6.27	1.9	1.8	2.56	1.59	631
BPFO75	3.55	1.57	8.55	2.72	13	10.6	3.61	0.36	649
BPFO10	6.73	2.63	5.06	1.57	34	12	0.86	0.11	629

Table 2.
Values of spontaneous polarization (P_s), remanent polarization (P_r), electric coercivity (E_c), current density (J) at 20 kV cm^{-1}, dielectric constant (ε) and MC at 1 kHz and 1 MHz, and ferroelectric phase transition (T_{FE}) at 1 MHz for $Bi_{1-x}Pb_xFeO_3$ [x = 0 (BFO), 0.05 (BPFO5), 0.075 (BPFO75) and 0.1 (BPFO10)] nanostructures [11].

free electrons. It resulting into a higher conductivity and hence have a harmful influence on the ferroelectricity. The Pb doping into BFO could increase the grain size as well the oriented growth (nanorod-type) in the samples. From **Table 2**, there is a considerable reduction in the leakage current of BFO upon Pb^{2+} doping, which indicates reduction in oxygen vacancies.

3.3.2 Ferroelectric and piezoelectric properties of epitaxial $BiFeO_3$ thin film

Figure 5(a) and **(b)** shows the ferroelectric polarization and piezoelectric behavior of epitaxial $BiFeO_3$ thin film [35]. The films display a room-temperature spontaneous polarization (50 to 60 μC cm^{-2}) almost an order of magnitude higher than that of the bulk (6.1 μC cm^{-2}). These results leads to the observations of

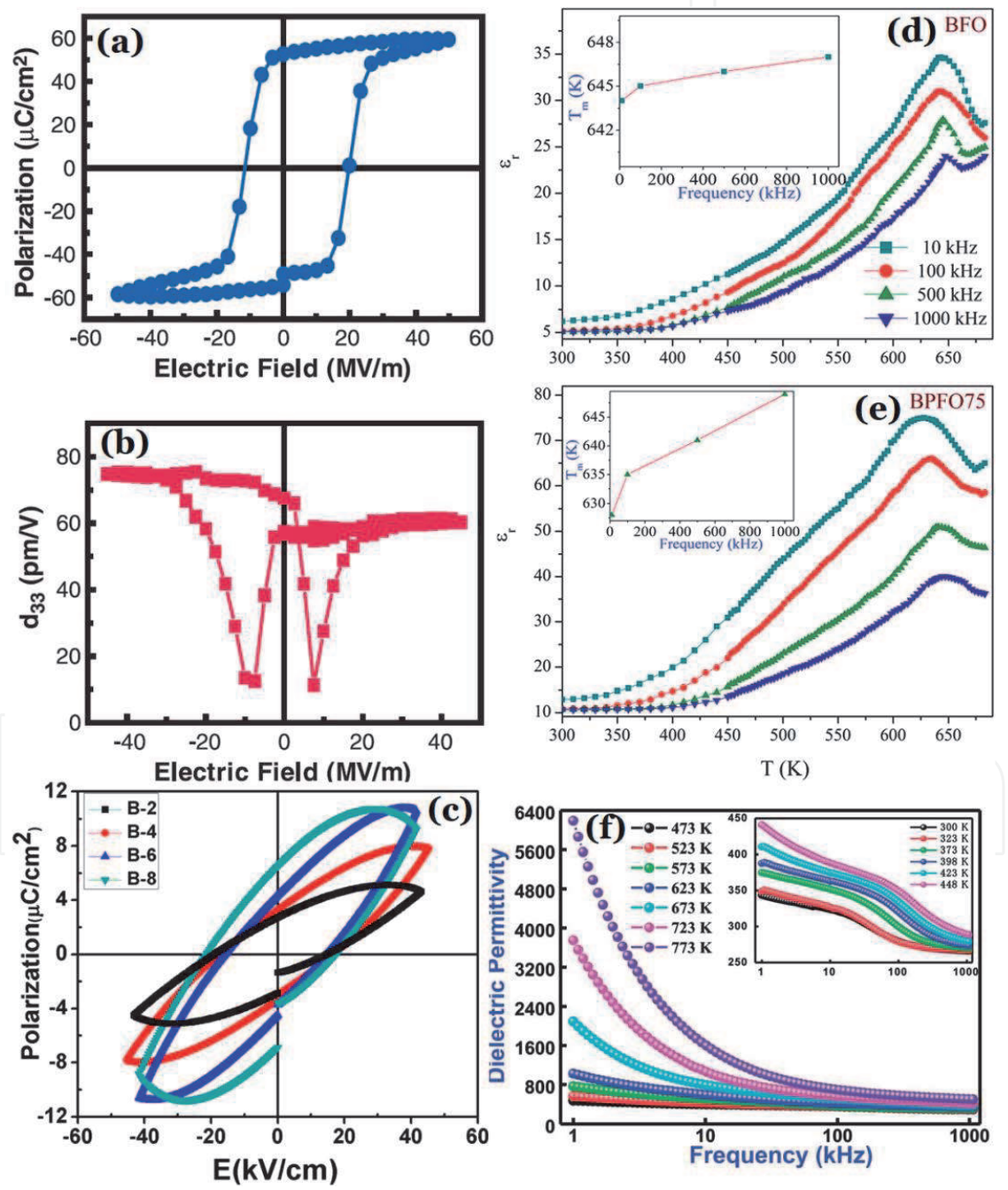

Figure 5.
(a) A ferroelectric hysteresis of $BiFeO_3$ thin film at 15 kHz. (b) a small signal d_{33} for a 50-μm capacitor [35]. (c) Room temperature PE loops of $BaTiO_3/BiFeO_3/BaTiO_3$ trilayer thin films having different $BiFeO_3$ thicknesses [36]. Temperature dependent relative permittivity (ε_r) of (d) $BiFeO_3$ (e) $Bi_{0.925}Pb_{0.075}FeO_3$ [11]. (f) Frequencies dependent dielectric permittivity at different temperatures for $Bi(Co_{0.4}Ti_{0.4}Fe_{0.2})O_3$ (insets shows lower temperature behavior) [37].

heteroepitaxial, in-plane compressive stress imposed by the epitaxial bottom electrode allows growth of a monoclinic crystal structure in BFO, and the degree of compressive stress progressively decreases with increasing BFO thickness. The piezoelectric hysteresis loop shows a remanent out-of-plane piezoelectric coefficient (d_{33}) value 70 pm V^{-1}, representing the piezoresponse of the film in the fully clamped state.

3.3.3 Ferroelectric hysteresis of $BaTiO_3/BiFeO_3/BaTiO_3$

Figure 5(c) represents polarization hysteresis loops of trilayer films of $BaTiO_3/BiFeO_3/BaTiO_3$ measured at 50 kV cm^{-1} applied electric field frequency of 10 kHz [36]. This trilayer thin film was prepared by RF-magnetron sputtering technique at different thicknesses of $BiFeO_3$ layer. The thickness of BTO layer is 20 nm at the top and bottom, and the middle layer BFO is deposited with thicknesses of 20 nm (B-2), 40 nm (B-4), 60 nm (B-6), and 80 nm (B-8), respectively. The film showed maximum remnant electric polarization ($2P_r$) of 13.5 μC cm^{-2} and saturation magnetization (M_s) of 61 emu cc^{-1} at room temperature. The ferroelectric polarization was found to be improved with increasing thickness of BFO layer may be attributed to the reduced oxygen vacancies.

3.4 Dielectric properties of $BiFeO_3$

3.4.1 Frequency dependent dielectric properties of $Bi(Co_{0.4}Ti_{0.4}Fe_{0.2})O_3$

Figure 5(f) correlates the dielectric permittivity versus frequency plot at temperatures from 300 to 773 K of $Bi(Co_{0.4}Ti_{0.4}Fe_{0.2})O_3$ multiferroic [37]. As the value of dielectric permittivity decreases upon increasing frequency, its nature could be described by Koop's hypothesis and Maxwell-Wagner mechanism. The nano grains with highly resistive grain boundaries might exist in an inhomogeneous medium from which the application of electric field constructs space charge polarization. With low frequency, the grain boundaries influence is more dominant to cause dispersion in dielectric properties. However, the higher frequency reduces the space charge polarization impact because the slow traveling species are not capable to trace an applied electric field.

3.4.2 Temperature dependent dielectric permittivity of $Pb:BiFeO_3$

Figure 5(d) and **(e)** shows the temperature dependent relative permittivity (ε_r) for $BiFeO_3$ and $Bi_{0.925}Pb_{0.075}FeO_3$ (BPFO75) multiferroics [11]. The value of ε_r starts to increase with temperature because of T_C for pure BFO is 1103 K. This change in ε_r at 600-650 K for both Pb:BFO samples occurs due to occurrence of T_N. For pure BFO, the value of T_N is 643 K. The value of the ferroelectric phase transition (T_{FE}) is 644 and 649, respectively, for BFO and BPFO75. This observation is an anomaly in the phase transition; T_{FE} around T_N confirms the ME coupling, which must be correlated with inverse DM-type interactions and Landau-Devonshire theory of phase transition. The variation in phase transition temperature with frequency for Pb:BFO nanostructures (inset of **Figure 5(d)** and **(e)**) indicates the emergence of the relaxor behavior which explained with an increase cation disorder in the B-site and Bi-site substitution by Pb^{2+}.

3.5 Magnetization in $BiFeO_3$

The magnetization of $BiFeO_3$ is reported in the refs. [39–44]. The cycloidal model of spin ordering in BFO is distorted at low temperatures. Any break to the

cycloidal spin structure could induce uncompensated spins, enhancing the magnetization [45].

3.5.1 Magnetization in multiferroic $BiFeO_3$ and $Bi_{0.9}Pb_{0.1}FeO_3$

The ferromagnetic behavior of Pb substituted $BiFeO_3$ is reported in ref. [11] that the maximum value of magnetization, M = 4.73, 8.41, 2.62 and 8.99 emu g^{-1}, respectively, for BFO, BPFO5, BPFO75 and BPFO10. The origin of the variation of magnetization is analyzed with temperature dependent zero field (ZFC) and field cooled (FC) magnetization is shown in **Figure 6(a)**. The splitting of the ZFC/FC curves usually appears as the co-existent system of the antiferromagnetic and ferromagnetic phases. With nanostructural dimensions of less than 62 nm, there is a possibility of modification to the cycloidal spin structure of BFO, and that can lead to weak room temperature ferromagnetism. The sharp cusp observed around 65 and 79 K, respectively, for BFO and BPFO10 nanostructures in the ZFC curve is represented by the blocking temperature (T_B which may attribute via superparamagnetic relaxation, glass transition, T_N for antiferromagnetic-

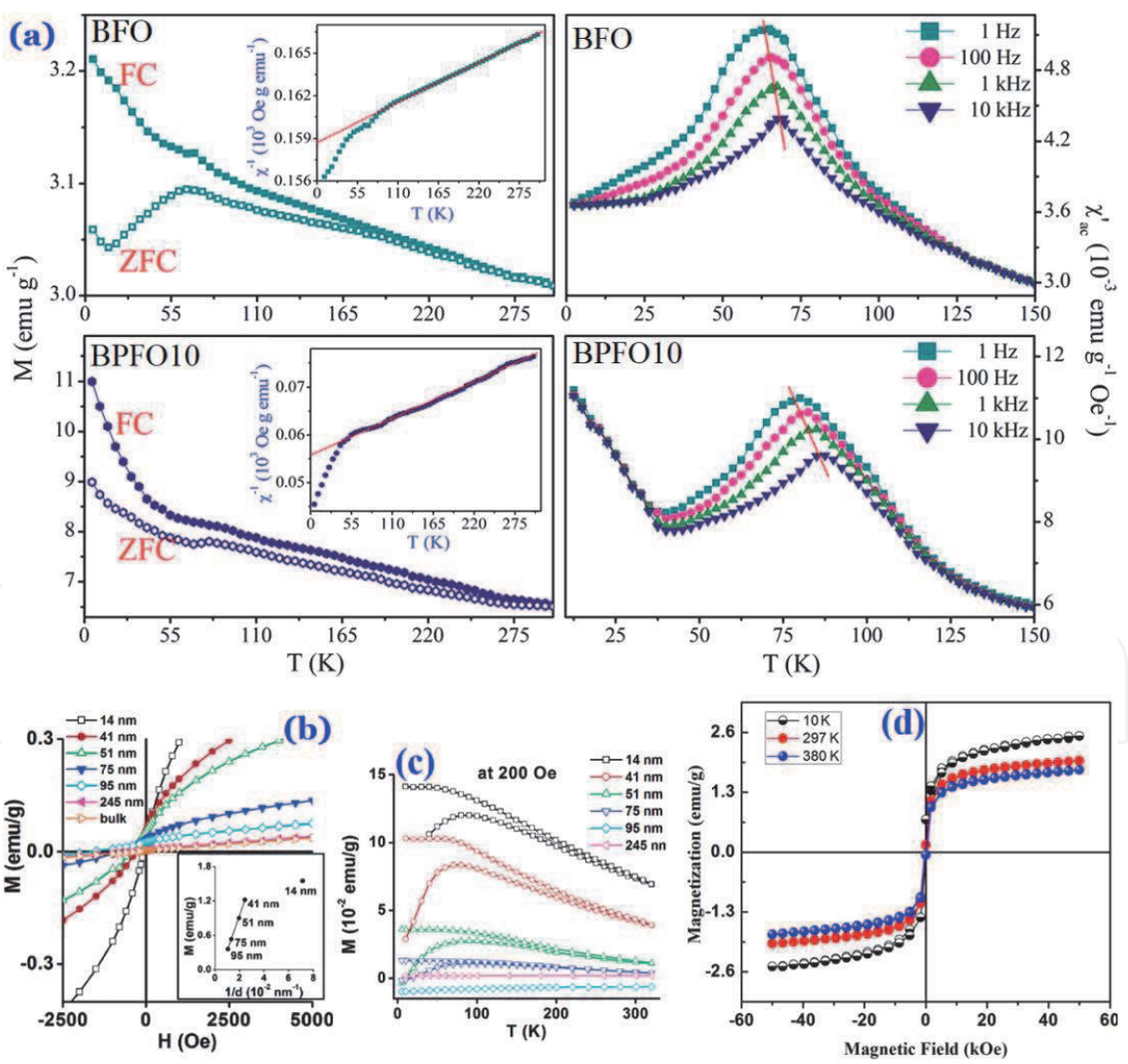

Figure 6.
(a) Magnetization (M) as a function of temperature (T) following ZFC and FC at H = 500 Oe for $BiFeO_3$ (BFO) and $Bi_{0.9}Pb_{0.1}FeO_3$ (BPFO10) multiferroics. The respective insets are $\chi^{-1}(T)$ following Curie-Weiss law. (a: right) The temperature dependent real part of the ac *magnetic susceptibility (χ'_{ac}) at T = 5-200 K (H_{ac} = 2.5 Oe without any dc field bias) [11]. (b) Magnetic hysteresis at 300 K for $BiFeO_3$ nanoparticles with different nano-sizes. Inset shows the corresponding magnetization at 50 kOe as a function of* 1/d*. (c) Respective ZFC and FC curves at 200 Oe [39]. (d) Magnetic hysteresis of $BiFeO_3$ nanoparticles grafted on graphene nanosheets ($BiFeO_3$-g-GNS) [40].*

ferromagnetic transition). The enhancement in magnetization is explained by Coey JMD *et al.* [46] model of F-center exchange mechanism where spin-polarized electrons were trapped at oxygen vacancies to cause higher magnetic moments. The upward curvature in FC curve of M(T) measurements of Pb:BFO suggested a Curie-Weiss like behavior **Figure 6(a)** (inset). The estimated value of θ is found to be negative which indicate to the formation of antiferromagnetic interactions.

The *ac* magnetic susceptibility of Pb substituted BFO is measured at 1 Hz, 100 Hz, 1 kHz 10 kHz, and the temperature dependent real (χ'_{ac}) *ac* magnetic susceptibility (χ_{ac}) is shown in **Figure 6(a)**(right). The applied oscillating field, H_{ac} = 2.5 Oe without any *dc* bias in T = 5-200 K. A quite sharp cusp is observed in both the samples. This *ac* magnetic measurement at different frequencies revealed the peak positions of χ'_{ac}(T) curve shift toward higher temperature and the peak magnitudes drop down with rising frequency. Such behavior is expected for a spin glass system. The dynamic susceptibility measurements can thus be used to confirm such spin glass or superparamagnetic by using frequency dependence of $T_f(\omega)$ in the expression, $\Delta p = \frac{\Delta T_f}{T_f \Delta(\log \omega)}$. The calculated peak shift (Δp) per decade of frequency shift has a value 0.014 and 0.019, respectively, for BFO and BPFO10. These values of Δp are lower than those observed for superparamagnetic system (Δp is ~0.1.54).

3.5.2 Nano size dependent magnetism of $BiFeO_3$

The SQUID results as shown in **Figure 6(b)** suggest that a magnetic response in $BiFeO_3$ can be initiated when the size of the system is less than about 95 nm [39]. A plot of the magnetization, measured at the maximum applied field of $H_{appl} \sim 50$ kOe as a function of 1/d, is given (inset of **Figure 6(b)**). Neel L [47] attributed the magnetic moment of small antiferromagnetic particles for the incomplete magnetic compensation between these two spin sublattices. For single-domain antiferromagnetic particles, the magnetization is expected to scale as ~1/d(diameter), that is, as the surface to volume ratio [39]. For particles ranging in diameter from 95 to 41 nm, a linear dependence is observed, indicating that the simple Neel model is applicable [48]. The smallest nanoparticle is 14 nm that deviates from the expected behavior which indicates that such 14 nm nanoparticle may diminish the model for superposition of an antiferromagnetic core and a ferromagnetic surface. The maximum magnetization, obtained as $M_s \sim 1.55$ emu g^{-1} for the 14 nm particles. **Figure 6(c)** shows the magnetization measurements as a function of temperature at an applied field strength of 200 Oe following ZFC and FC process. It is noted that the apparent sharp cusps observed in the magnetization curves at 50 K are reproducible for BFO samples with particle dimensions over 95 nm (e.g. 245 nm and bulk). For $BiFeO_3$ nanoparticles possessing diameters of ≤95 nm, associated data curves exhibit a broad magnetization maximum around T_{max} = 85 K. T_{max} represents a spin-glass-like freezing temperature due to high packing volume fraction as well as a complex interplay between finite size effects, interparticle interactions, and a random distribution of anisotropy axes.

3.5.3 Temperature dependent magnetization of $BiFeO_3$-g-GNS nanoparticles

Magnetic properties of $BiFeO_3$ grafted on graphene nanosheets ($BiFeO_3$-*g*-GNS) is studied using SQUID VSM with an applied field of 5 T at different 10, 297 and 380 K **Figure 6(d)** [40]. Magnetic moments of nanoparticles get distorted at higher temperature. The maximum observed value of magnetization is 2.52 emu g^{-1} at 10 K, while the minimum is 1.78 emu g^{-1} at 380 K. At room temperature,

magnetization measured to be 1.98 emu g^{-1}. These values well matched with reported data [49]. It means the magnetic properties of $BiFeO_3$ are not compromised on GNS grafting.

3.5.4 Magnetization of $BiFeO_3$-$CoFe_2O_4$ (BFO-CFO) bulk heterojunction

Figure 7(a) exhibits the magnetic hysteresis in isotropic magnetic behavior along in plane and out of plane directions [41]. The value of M_s of BFO-CFO/mica is ~237 emu cm^{-3} with $H_c \sim 2$ kOe, which is smaller than from epitaxial CFO/STO (~3 kOe). This may due to the effect of an effective relaxation of clamping from the mica substrate.

3.5.5 Ferromagnetism in $BiFeO_3$/$BaTiO_3$ bilayer interface

Figure 7(b) shows the ferromagnetic behavior of $BiFeO_3$/$BaTiO_3$ (BTO thickness = 100 nm; BFO = 50 nm (BFBT-5), 100 nm (BFBT-10), 150 nm (BFBT-15), and 200 nm (BFBT-20) films [30]. The observed ferromagnetism in the bilayer thin films can be interpreted due to creation of unbalanced spins at the interface. Maximum magnetization value $M_s \sim 33$ emu cc^{-1} was observed in BFBT-5. The value of saturation magnetization is 20 emu cc^{-1} for BFBT-10 sample which is higher than for those observed in BFBT-15 (15 emu cc^{-1}) and BFBT-20 (8 emu cc^{-1}). This is because with smaller antiferromagnetic nanoparticles, the size reduction has incomplete surface compensation of long-range antiferromagnetic ordering which result into increase magnetic moment at comparatively smaller size nanograins.

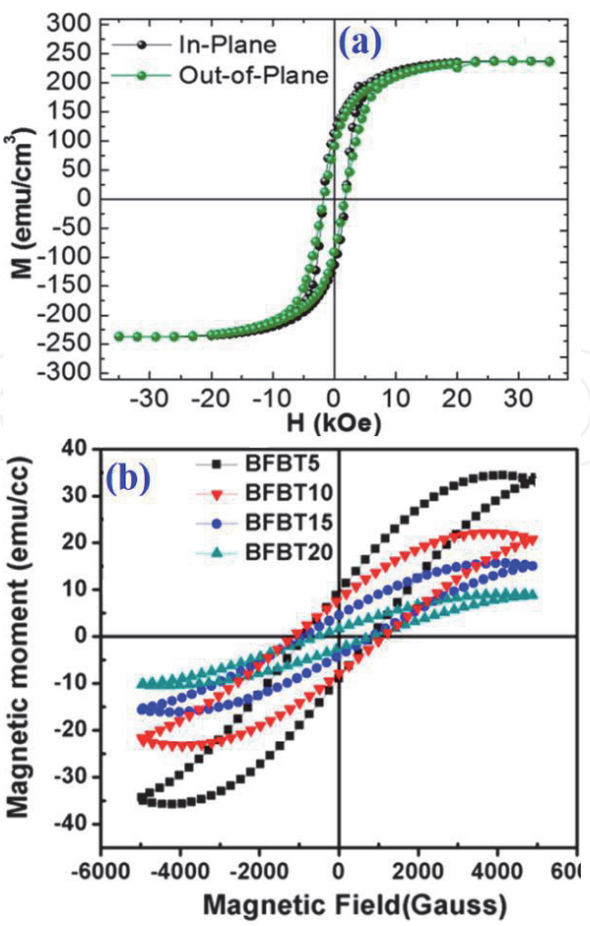

Figure 7.
(a) M-H hysteresis for $BiFeO_3$-$CoFe_2O_4$ composite at room temperature [41]. (b) M-H loops of bilayer $BiFeO_3$/$BaTiO_3$ thin films [30].

3.6 Magnetocapacitance

The ME behavior due to Magnetocapacitance (MC) effect in $BiFeO_3$ is given in the refs. [50–54]. The MC effect is the change in the capacitance with an external applied magnetic field. This MC/magnetodielectric effect has a resistive origin that arises from the Maxwell-Wagner effect and magnetoresistance [55].

3.6.1 Dielectric constant and MC of Pb substituted $BiFeO_3$

Table 2 shows the magnetic field affected dielectric constant of Pb:BFO nanostructures measured at room temperature. The frequency dependent relative permittivity (ε_r) of Pb:BFO in the frequency region 20 Hz-10 MHz under *dc* magnetic field (H = 0, 1 kOe) is given [11]. From **Table 2**, the improvement in dielectric constant with the substitution of Pb^{2+} for Bi^{3+} provides a larger vibration space to a larger dipole moment. Besides the oxygen vacancies due to ionic formation of Fe^{2+}/Fe^{3+} valence states, the shape/size of BFO grains might to influence the dielectric behaviors [11]. It is also observed from **Table 2** that the capacitance varies with applying magnetic field of 1 kOe, which indicate a positive/negative MC effect. The applied magnetic field leads to local stresses (or strains) and consequently changes in the polarization of the ferroelectric phase due to the piezoelectric effect. The values of MC $\{[\varepsilon(H) - \varepsilon(0) = \Delta\varepsilon]/\varepsilon(0)\}$ at a frequency of 1 MHz is 0.61, 1.59, 0.36 and 0.11%, respectively, calculated for BFO, BPFO5, BPFO75 and BPFO10 multiferroic.

3.6.2 Magnetocapacitance effect in $BiFe_{0.95}Sc_{0.05}O_3$

The magnetic field dependent capacitance for $BiFe_{0.95}Sc_{0.05}O_3$ system to induce MC effect at 30 kHz is shown in **Figure 8(a)** [50]. The value of MC is 0.04% at applied magnetic field of 5 T which is higher than from pure BFO (0.007%). This type of MC behavior might be correlated with P^2M^2 in a Ginzburg-Landau free energy leads to a quadratic dependent dielectric constant in respect to magnetization. The observed results of MC in **Figure 8(a)** have magnetization-linear dielectric behavior which may proportional to P^2M of a linear MC effect.

3.6.3 Piezoelectric properties of $BiFeO_3/Na_{0.5}Bi_{4.5}Ti_4O_{15}$ composite films

Lead-free $BiFeO_3/Na_{0.5}Bi_{4.5}Ti_4O_{15}$ (BFO/NBTO) composite films were deposited on Pt(100)/Ti/SiO_2/Si substrates using chemical solution deposition [51]. A giant ME voltage coefficient has maximum α_E = 136 mV cm^{-1} Oe^{-1} at H_{bias} = 8.0 kOe. **Figure 8(b)** shows the piezoelectric coefficient (d_{33}) and surface displacement (d) vs. applied voltage (V) for BFO/NBTO films. A typical butterfly curve from D-V characteristics shows maximum value 4.06 nm at 15 V of 2.63% highest ratio of strain. The occurrence of d_{33}-V piezoelectric hysteresis from D-V curve is the result converse piezoelectric effect. The d_{33}-V loop clearly shows that BFO/NBTO composite films are switchable and the ferroelectricity is retained. The piezoelectric coefficient d_{33} of BFO/NBTO films is as high as 285 pm V^{-1} at 20 V, which suggests the strong piezoelectric effect for BFO/NBTO films.

3.6.4 Magnetostriction of $BiFeO_3$-$BaTiO_3$, $Bi_{0.8}FeO_{2.7}$-$BaTiO_3$, and $BaFe_{12}O_{19}$

The magnetostriction of BFO-BTO, $B_{0.8}FO_{2.7}$-BTO, and $BaFe_{12}O_{19}$ ceramics was measured using a resistive strain gauge when a dc magnetic field was applied to the materials (**Figure 8(c)**) [52]. A contraction induced by the magnetic field is

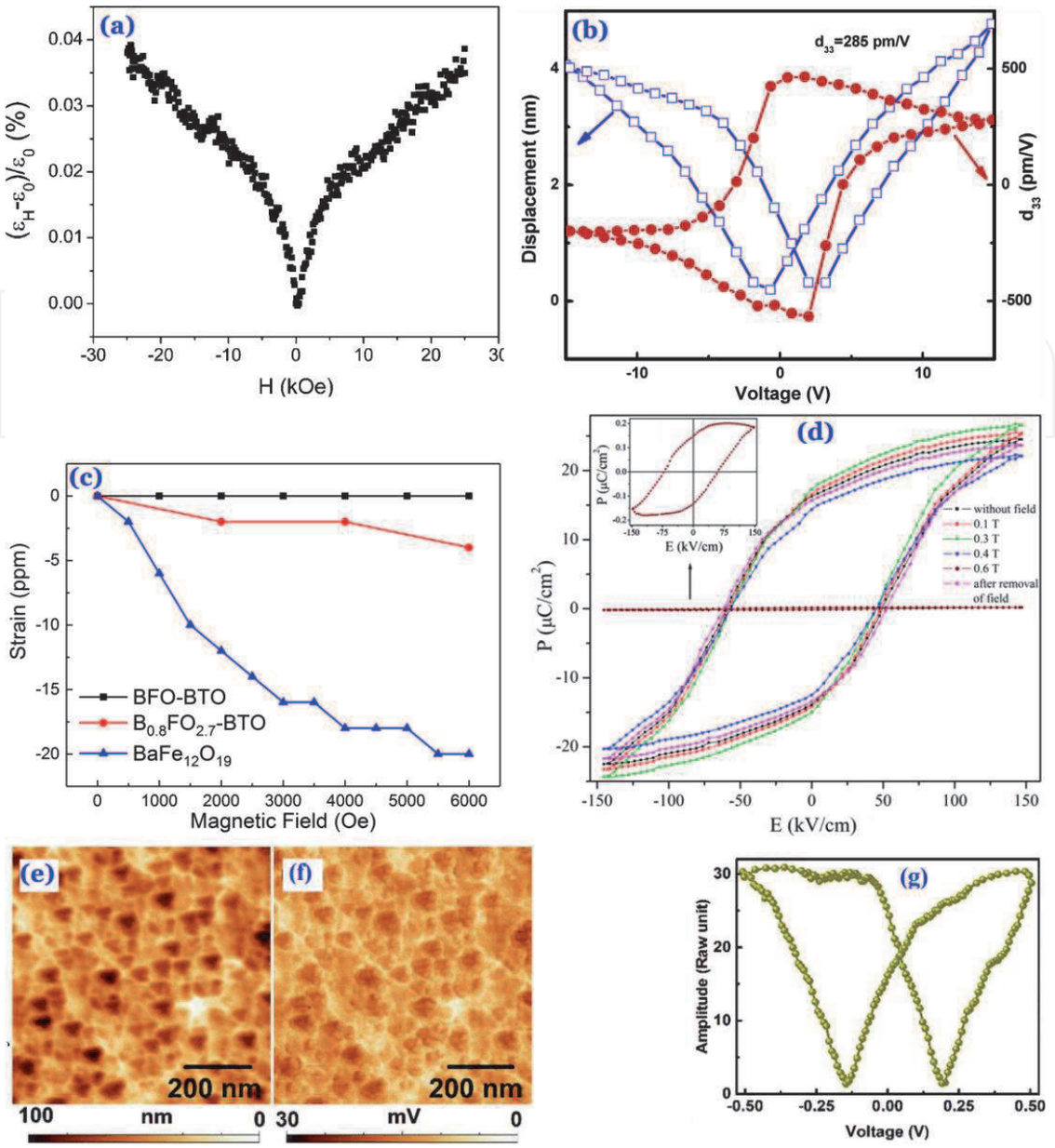

Figure 8.
(a) Magnetocapacitance of $BiFe_{0.95}Sc_{0.05}O_3$ [50]. (b) Piezoelectric response of $BiFeO_3/Na_{0.5}Bi_{4.5}Ti_4O_{15}$ (BFO/NBTO) composite [51]. (c) Magnetostriction of $BiFeO_3$-$BaTiO_3$, $Bi_{0.8}FeO_{2.7}$-$BaTiO_3$, and $BaFe_{12}O_{19}$ measured at room temperature [52]. (d) P-E hysteresis under 0-0.6 T field for BFO-BTO nanoparticles. (Inset of d) P ~ 0 at 0.6 T [53]. PFM study on $BiFeO_3$ thin film: (e) AFM (f) amplitude image (g) amplitude behavior at an applied bias [54].

observed, and at 6 kOe, the contraction is approximately 20 ppm. $BaFe_{12}O_{19}$ is a ferromagnetic material and can have a magnetostrictive response. However, due to the weak ferromagnetic nature of the BFO-BTO ceramics, it was difficult to detect the strain below 6 kOe. Because only a small amount of $BaFe_{12}O_{19}$ is generated in the Bi-deficient ceramics, the magnetostriction is also very small in the materials.

3.6.5 ME coupling: ferroelectric polarization in an applied magnetic field

The mechanism for the spin driven ferroelectricity must be involved the spin-current model or inverse DM interaction due to the local electric polarization, $p \propto e_{ij} \times (S_i \times S_j)$, where e_{ij} is the unit vector of adjacent spins, S_i and S_j [56]. These cycloidal spin structures produced the macroscopic electric polarization P due to helicity of spins. The ferroelectric hysteresis under an external magnetic field and the flop near 0.6 T reveal a strong ME coupling in BFO-BTO multiferroics as shown

in **Figure 8(d)** [53]. Without applying H, values of P_{max} = 24.80 μC cm^{-2}, P_r = 15.13 μC cm^{-2} and E_c = 53.6 kV cm^{-1} are observed. Switching from $+P_r$ to $-P_r$ by E, and magnetic switching from $+P_r$ to zero at 0.6 T have been observed. The inset of **Figure 8(d)** shows a low polarization response with lossy hysteresis of BFO-BTO composite at 0.6 T, which may cause by the electrode. When a magnetic field is applied to a ME material, the material is under strain to induce a stress on the piezoelectrics (ferroelectric) to orient ferroelectric domains, leading to enhance polarization.

3.6.6 ME effect in $BiFeO_3$ by PFM

Figure 8(e) shows AFM, out of plane piezoresponse amplitude of the BFO thin film which leads to agglomeration of the nanoparticles of average size 10 nm [55]. It can be seen from **Figure 8(f)** that BFO nanoparticles exhibits positive and negative polarization components and the ferroelectric domains are constrained at grain boundaries. The PFM amplitude under bias voltage is shown in **Figure 8(g)**. It observed ferroelectric hysteresis for dc voltage sweeps in +0.5 V to −0.5 V to +0.5 V which indicates that sub - 5 nm BFO nanoparticles retains their ferroelectric behavior that might be usable for read-write operation.

3.7 Magnetoelectric (ME) coupling

3.7.1 ME coupling in $Bi_{0.88}Dy_{0.12}Fe_{0.97}Ti_{0.03}O_{3+\delta}$ (BDFO) and $BiFeO_3$

The ME effect of BFO and BDFO was measured, and the results are shown in **Figure 9(a)** [57]. It can be seen that the pure $BiFeO_3$ exhibits no ME signal under bias magnetic field because spatially incommensurately modulated spin structure that cancels out the linear ME effect. In contrast, BDFO exhibits a strong ME signal under bias magnetic field at 300 K due to the ME coefficient α_E-magnetic field (α_E-H) hysteresis to include the features of saturation at field of 250 Oe. This is because the switching of electric polarization by either 109° or 71° leads to switching of the ferroelastic domain states [58–60]. The incorporation of Dy^{3+} into BFO suppresses the spiral spin structure, leads to weak ferromagnetism. Because the magnetic moment lags behind the variation of magnetic field, the electric polarization induced by magnetic field through ME effect is also lagged behind the variation of magnetic field, giving α_E(H) hysteresis.

3.7.2 ME coupling of 15 × (10 nm $BaTiO_3$-5 nm $BiFeO_3$)

The ME coefficient was measured as a function of dc bias field in **Figure 9(b)** for 15 × (10 nm $BaTiO_3$-5 nm $BiFeO_3$) [58]. The ME coefficient reaches its maximum, off - resonance, value of 60.2 V cm^{-1} Oe^{-1} at a bias field of 2 T. This higher value is described due to the rotation of the oxygen octahedra with the antiferrodistortion vector Ω and shows that the linear ME effect depends on the derivative of Ω with respect to the external field. This leads to giant values of α_{ME}.

3.7.3 ME coupling of 15 × [$BaTiO_3$/$BiFeO_3$] multilayer

The effect of strain and interfaces on the ME coupling in $BiFeO_3$ was studied for a number of thin films and multilayers of 15 × [$BaTiO_3$/$BiFeO_3$] as shown in **Figure 9(c)** [33, 59]. To this end, a direct longitudinal ac method was used to measure the ME coefficient α_{ME} as a function of static magnetic field. It is clear that α_{ME} of the multilayer is notably larger than that of the BFO film. Since the

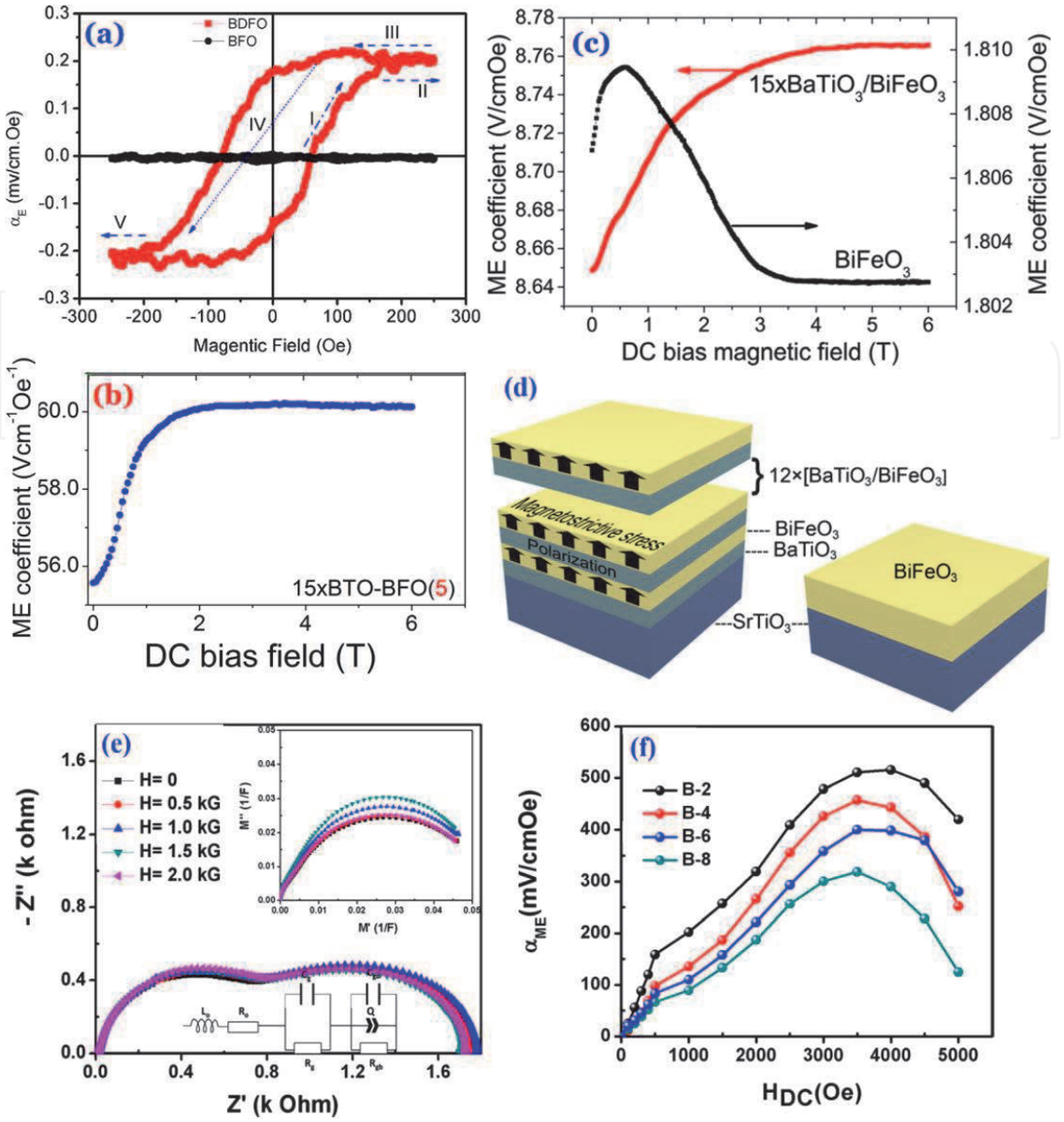

Figure 9.
(a) Magnetoelectric P(H) hysteresis at 300 K, showing ME coefficient of $Bi_{0.88}Dy_{0.12}Fe_{0.97}Ti_{0.03}O_{3+\delta}$ (BDFO) and BFO multiferroic [57]. (b) ME coefficient of the multilayers 15 × (10 nm $BaTiO_3$ - 5 nm $BiFeO_3$) at room temperature [58]. (c) ME coefficient α_{ME} of 15 × [$BaTiO_3$/$BiFeO_3$] multilayer film and pure $BiFeO_3$. (d) Ferroelectric-multiferroic multilayer (left) showing the ME effect through magnetostrictive-piezoelectric interface coupling (arrows represent magnetostrictive stress); and a $BiFeO_3$ film (right) [59]. (e) ME-impedance response of $BaTiO_3$/$BiFeO_3$/$BaTiO_3$ trilayer film measured at room temperature (magnetomodulus plots: inset). (f) ME coefficient for BTO/BFO/BTO trilayer films [36].

multilayer additionally contains piezoelectric/piezomagnetic interfaces, an extra ME coupling in multilayers may occur via the horizontal interfaces through strain-mediated interface coupling. The magnetostrictive stress is produced in the weak ferromagnetic $BiFeO_3$ layer and is transferred to ferroelectric $BaTiO_3$ layer through the interface (**Figure 9(d)**). This mechanical stress generates an electric potential difference in the ferroelectric layer via a piezoelectric effect.

3.7.4 Magnetoimpedance and ME effects of $BaTiO_3$/$BiFeO_3$/$BaTiO_3$ heterostructure

The ME effect for $BaTiO_3$/$BiFeO_3$/$BaTiO_3$ heterostructure is also investigated by analyzing complex impedance (−Z″ vs. Z′) as well as complex modulus plots (M″ vs. M′) under applied magnetic fields (**Figure 9(e)**) [36]. The data were fitted with an equivalent circuit of two series RC-elements. Two well resolved semicircles

$BiFeO_3$ composition	Synthesis method	Phase structure	Nano-structure	P_s/P_r ($\mu C\ cm^{-2}$)	M ($emu\ g^{-1}$)	MC (%)	α_{ME} $mVcm^{-1}\ Oe^{-1}$	Ref.
$BiFeO_3$	Pulsed laser deposition	M	70 nm thick film	60/55	150	—	3000	[35]
$BiFeO_3$	Chemical-solution deposition	R	140 nm thick film	125/73	—	—	—	[61]
$BiFeO_3$	Hydrothermal synthesis	R	20 nm square nanosheets	~4.2/3	3.1	—	—	[62]
$BiFeO_3$	Chemical combustion	R	D = 75 nm	0.75/0.35	0.73	0.68	—	[11]
$BiFeO_3$	PVA sol-gel	R	—	2.9/2.13	0.624	0.6	3.37	[63]
$Bi_{0.9}Ba_{0.1}Fe_{0.9}Mn_{0.1}O_3$	Mechano-synthesis	R	D = 1 μm	~1.1/0.82	AF	—	~74	[64]
$Bi_{0.9}Eu_{0.1}FeO_3$	Sol–gel	Distorted R	D = 27 nm	10.5/5.1	~0.7	11.9	—	[65]
$Bi_{0.9}Sm_{0.1}FeO_3$	Sol–gel	Distorted R	D = 28.5 nm	15.1/7.2	AF	~17	—	[66]
$BiFe_{0.925}Sc_{0.05}Ti_{0.025}O_3$	Sonochemical	Distorted R	D = 20-25 nm	2.63/1.03	0.34	0.05		[67]
$Bi_{0.9}Sm_{0.1}Fe_{0.95}Co_{0.05}O_3$	Sol–gel/pulsed laser deposition	R	300 nm thick film	22.91/16.1	35	—	142	[68]
$BiFe_{0.92}Mn_{0.08}O_3$	Solution-gelation technique (thin film)	R	D = 23.96 nm	23.56/9.5	—	—	—	[69]
$Bi_{0.9}Y_{0.1}FeO_3$	Spin coating deposition	R	D = 90-105 nm	—	2.87	—	—	[70]
$BiFe_{0.9}Co_{0.09}Mn_{0.01}O_3$	Hydrothermal route	R	—	—	10.88	—	7.4	[71]
$0.33Ba_{0.7}Ca_{0.3}TiO_3$-$0.67BiFeO_3$	Conventional sintering method	T/R	D = 12 μm	15/9.1	0.33	2.96	—	[72]
$(Bi_{1/2}Ba_{1/4}Sr_{1/4})(Fe_{1/2}Ti_{1/2})O_3$	Thermo-mechanical	R	D = 5-20 nm	~12/0.6	~0.05	—	8.7	[73]
$BaTiO_3$–$BiFeO_3$–$LaFeO_3$	Sol–gel	O	D = 1-2 μm	~2.5/0.14	0.67	—	354	[74]
5% $BiFeO_3$–$NaNbO_3$ in P (VDF-TrFE)	Spin coating	α & β phases of PVDF	D = 100-150 nm	8/2	0.03	—	2400	[75]
$0.75(Bi_{0.99}\ La_{0.01})FeO_3$-$0.25BaTiO_3$	Conventional solid state	R/C	Core-shell	~35/27	~0.6	—	~3.4	[76]
$0.9BiFeO_3$-$0.1BaTiO_3$	Sol–gel	R	D = 186 nm	~0.15/0.1	AF	—	2.74	[77]

$BiFeO_3$ composition	Synthesis method	Phase structure	Nano-structure	P_s/P_r ($\mu C\ cm^{-2}$)	M ($emu\ g^{-1}$)	MC (%)	α_{ME} $mVcm^{-1}\ Oe^{-1}$	Ref.
$0.5BiFeO_3/0.5MnFe_2O_4$	Sol–gel auto-combustion	R/spinel	D = 110 nm	0.64/0.97	15.65	—	—	[78]
$BiFeO_3/BiMnO_3$	Pulsed laser	Pseudo-cubic	Superlattices: ~32 nm thick	26	10	—	—	[79]
$BiFeO_3-BaTiO_3$	RF-magnetron sputtering	(110) plane: high degree	50 nm thick $BiFeO_3$	15.5/9	33	4.96	61	[30]
$0.7BiFeO_3/0.3MgLa_{0.025}Fe_{1.975}O_4$	Sol–gel auto combustion	distorted R	D = 56 nm	0.28/0.08	5.28	—	—	[80]
$0.9BiFeO_3$-$0.1PbTiO_3$	Sol–gel solid state	R/T	—	3.8×10^{-5}	0.06	—	0.2	[81]
$BaFe_{12}O_{19}/BiFeO_3$	Mechano-chemical	H/R	D = 588 nm	~2.8/1.4	~28	—	11.9	[82]
$BiFeO_3/CoFe_2O_4$	Solvothermal	R/spinel	D = 285 nm	2.1/1	30.1	—	8.5	[83]
$0.7BiFeO_3$-$0.3PbTiO_3$	Solid-state	R/T	D = 37 nm	~1.1/0.2	AF	—	—	[84]
$0.67BaTiO_3–0.33BiFeO_3$	Pulsed laser	R/T	1850 nm thick film, D = 40 nm	$400/230 \times 10^{-2}$ Cm^{-2}	$2 \times 10^{-3}\mu_oT$	—	20.75	[33]
$BaTiO_3/BiFeO_3/BaTiO_3$	RF-magnetron sputtering	R/T	BTO = 20 nm BFO = 40 thick thin film	~8/3.2	37	5.95	457	[36]
$Bi_{0.8}FeO_{2.7}$-$BaTiO_3$	Solid-state	R/T	D = ~1 μm	~48/30.2	~5.5	—	~120	[52]
$BiFeO_3/Na_{0.5}Bi_{4.5}Ti_4O_{15}$	Chemical solution deposition	R/O	BFO = 879 nm NBT = 545 nm	62.1/38.7	4.68	—	136	[51]

Table 3.
Summary of multiferroic properties of $BiFeO_3$ [phase structure (monoclinic (M), rhombohedral (R), tetragonal (T), orthorhombic (O), cubic (C), hexagonal (H)), nanostructural size (diameter (D) and length (l)), ferroelectric spontaneous polarization (P_s), remanent polarization (P_r), saturation magnetization (M), antiferromagnetic (AF), magnetocapacitance (MC), and magnetoelectric coefficient (α_{ME})].

representing increase in both grain and grain boundary resistance (R_g and R_{gb}) with applied magnetic field are shown. A maximum 20% increase in grain capacitance (C_g) with applied magnetic field of 2 kG to represent an intrinsic ME effect. The bonding between Fe and Ti atoms at interface results into ME interaction between BFO and BTO at both interfaces. This interaction to change grains/boundaries resistances with the application of magnetic field induced magnetoimpedance/MC effect which is explained with Maxwell-Wagner model consisting of two leaky capacitors connected in series.

The ME coefficient, α_{ME} was measured in trilayer $BaTiO_3/BiFeO_3/BaTiO_3$ film by dynamic method (**Figure 9(f)**) and the detailed measurement set-up is given [36]. The α_{ME} was calculated using equation, $\alpha_{ME} = \delta V/\delta H.t$, where δV is the measured output voltage, δH is applied ac magnetic field, and *t* is the film thickness. The maximum α_{ME} of ~515 mV cm^{-1} Oe^{-1} is observed for B-2 film. By increasing the thickness of BFO layer, α_{ME} found to be reduced to 457 mV cm^{-1} Oe^{-1} for B-4, 400 mV cm^{-1} Oe^{-1} for B-6, and to 318 mV cm^{-1} Oe^{-1} for B-8. The enhancement in ME coupling for trilayer films may the effect of bonding between Fe and Ti atoms at both interfaces via oxygen atom. The reduction in oxygen vacancies with increasing thickness of BFO layer results into decreasing α_{ME} value.

3.8 Comparison of multiferroic properties of $BiFeO_3$

In **Table 3**, we have reported the list of multiferroic properties such as synthesis method, phase structure, nanostructures, ferroelectric behavior, magnetization, magnetocapacitance and ME coefficient of $BiFeO_3$. It is observed that the single phase $BiFeO_3$ has multiferroic behavior enhanced due to different doping from transition and rare earth ions. For the composites of $BiFeO_3$, there are moderate improvements in ME coupling. However, for multilayer $BiFeO_3$ with $BaTiO_3$ or ferrites has remarkable value of ME coupling. The Magnetocapacitance effect study on $BiFeO_3$ is hardly reported. Therefore it is summarized that the different multi-layers perovskites structures of $BiFeO_3$ may give much advancement to the multiferroic behaviors.

4. Conclusion

Multiferroic $BiFeO_3$ becomes a suitable material for spintronic application of data storage. Wet chemical methods, hydrothermal, Polymer-directed solvothermal, sol–gel template process, sonochemical, anodized alumina template, sol–gel based electrospinning and microwave synthesis are the best synthesis routes to control the shape and size of $BiFeO_3$ nanostructures. These nanostructural shape and size of $BiFeO_3$ has much impact to control the magnetism and leakage current of $BiFeO_3$. In addition to change dopant level and composites with other materials (such as ferrites and other perovskites like $BaTiO_3$), the $BiFeO_3$ thin films especially multilayers gives remarkable results of ferroelectric polarization and ME voltage.

Acknowledgements

The author K.C. Verma thankfully acknowledges the financial support by UGC of Dr. DS Kothari Post Doctorate Fellowship [No. F4-2/2006(BSR)/PH/16-17/0066] and CSIR-HRDG for SRA (Pool Scientist) fellowship Grant No. B-12287 [SRA (Pool No): 9048-A].

Author details

Kuldeep Chand Verma[1,2]

1 CSIR-Central Scientific Instruments Organisation, Chandigarh 160030, India

2 Department of Physics, Panjab University, Chandigarh 160014, India

*Address all correspondence to: dkuldeep.physics@gmail.com; kcv0309@gmail.com

References

[1] Baibich MN, Broto JM, Fert A, Nguyen F, Dau V, Petroff F, Etienne P, Creuzet G, Friederich A, Chazelas J. Giant magnetoresistance of (001)Fe/(001)Cr magnetic superlattices. Phys. Rev. Lett. 1988; **61**, 2472-2475.

[2] Verma KC, Kotnala RK, Goyal N. Multi-Functionality of Spintronic Materials: Nanoelectronics. Elsevier; 2019; **eBook ISBN:** 9780128133545, 153-215.

[3] Sharma P, Zhang Q, Sando D, Lei CH, Liu Y, Li J, Nagarajan V, Seidel J, Sci. Adv. 2017; **3**: e1700512 (1-8)

[4] Tsymbal EY. Spintronics: Electric toggling of magnets, Nature Mater. 2012; **11**, 12-13

[5] Bibes M, Barthelemy A, Multiferroics Towards a magnetoelectric memory. Nature Mater. 2008; **7**, 425-426

[6] Scott JF. Data Storage Multiferroic memories. Nature Mater. 2007; **6**, 256-257

[7] Kent AD, Worledge DC. A new spin on magnetic memories. Nature Nanotechnology. 2015; **10**, 187-191

[8] Verma KC, Kotnala RK. Lattice Defects Induce Multiferroic Responses in Ce, La-Substituted $BaFe_{0.01}Ti_{0.99}O_3$ Nanostructures. J. Am. Ceram. Soc. 2016; **99[5]**, 1601-1608 (2016)

[9] Verma KC, Kumar M, Kotnala RK. Magnetoelectric, Raman, and XPS Properties of $Pb_{0.7}Sr_{0.3}[(Fe_{2/3}Ce_{1/3})_{0.012}Ti_{0.988}]O_3$ and $Pb_{0.7}Sr_{0.3}[(Fe_{2/3}La_{1/3})_{0.012}Ti_{0.988}]O_3$ nanoparticles. Metall. Mater. Trans. A. 2014; **45A**, 1409-1414

[10] Gajek M, Bibes M, Fusil S, Bouzehouane K, Fontcuberta J, Barthelemy A, Fert A. Tunnel junctions with multiferroic barriers. Nature mater. 2007; **6**, 296-302

[11] Verma KC, Kotnala RK. Tailoring the multiferroic behavior in $BiFeO_3$ nanostructures by Pb doping. RSC Adv., 2016; **6**, 57727-57738

[12] Fiebig M, Lottermoser T, Meier D, Trassin M. The evolution of multiferroics. Nature Rev.: Mater. 2016; **1**, 1-14

[13] Gross I, Akhtar W, Garcia V, Martinez LJ, Chouaieb S, Garcia K, Carretero C, Barthelemy A, Appel P, Maletinsky P, Kim JV, Chauleau JY, Jaouen N, Viret M, Bibes M, Fusil S, Jacques V. Real-space imaging of non-collinear antiferromagnetic order with a single-spin magnetometer. Nature 2017; **549**, 252-265

[14] Martin LW, Crane SP, Chu YH, Holcomb MB, Gajek M, Huijben M, Yang CH, Balke N, Ramesh R. Multiferroics and magnetoelectrics: thin films and nanostructures. J. Phys.: Condens. Matter. 2008; **20**, 434220 (1-13)

[15] Safi R, Shokrollahi H. Physics, chemistry and synthesis methods of nanostructured bismuth ferrite ($BiFeO_3$) as a ferroelectro-magnetic material. Prog. Solid State Chem. 2012; **40**, 6-15

[16] Selbach SM, Einarsrud MA, Tybell T, Grande T. Synthesis of $BiFeO_3$ by Wet Chemical Methods. J. Am. Ceram. Soc. 2007; **90 [11]**, 3430-3434

[17] Xu JH, Ke H, Jia DC, Wang W, Zhou Y. Low-temperature synthesis of $BiFeO_3$ nanopowders via a sol-gel method. J. Alloys Compd. 2009; **472**, 473-477

[18] Shami MY, Awan MS, Anis-ur-Rehman M. Phase pure synthesis of $BiFeO_3$ nanopowders using diverse precursor via co-precipitation method. J. Alloys Compd. 2011; **509**, 10139- 10144

[19] Liu B, Hu B, Du Z, Hydrothermal synthesis and magnetic properties of single-crystalline BiFeO3 nanowires. Chem. Commun., 2011, **47**, 8166–8168

[20] Manzoor A, Afzal AM, Umair M, Ali A, Rizwan M, Yaqoob MZ. Synthesis and characterization of Bismuth ferrite ($BiFeO_3$) nanoparticles by solution evaporation method. J. Magn. Magn. Mater. 2015; **393**, 269-272

[21] Li S, Zhang G, Zheng H, Wang N, Zheng Y, Wang P. Microwave-assisted synthesis of $BiFeO_3$ nanoparticles with high catalytic performance in microwave-enhanced Fenton-like process. RSC Adv., 2016; **6**, 82439-82446

[22] Joshi UA, Jang JS, Borse PH, Lee JS, Microwave synthesis of single-crystalline perovskite $BiFeO_3$ nanocubes for photoelectrode and photocatalytic applications. Appl. Phys. Lett. 2008; **92**, 242106-3

[23] Wu J, Mao S, Ye ZG, Xiea Z, Zheng L. Room-temperature ferromagnetic/ferroelectric $BiFeO_3$ synthesized by a self-catalyzed fast reaction process. J. Mater. Chem. 2010; **20**, 6512-6516

[24] Kim TC, Ojha S, Tian G, Lee SH, Jung HK, Choi JW, Kornblum L, Walker FJ, Ahn CH, Ross CA, Kim DH, Self-assembled multiferroic epitaxial $BiFeO_3$-$CoFe_2O_4$ nanocomposite thin films grown by RF magnetron sputtering. **J. Mater. Chem. C** 2018; **6**, 5552-5561

[25] Zhang L, Cao XF, Ma YL, Chen XT, Xue ZL, Polymer-directed synthesis and magnetic property of nanoparticles-assembled $BiFeO_3$ microrods. J. Solid State Chem. 2010; **183**, 1761-1766

[26] Wei J, Xue D, Xu Y, Photoabsorption characterization and magnetic property of multiferroic $BiFeO_3$ nanotubes synthesized by a facile sol-gel template process. Scripta Mater. 2008; **58**, 45-48

[27] Dutta DP, Jayakumar OD, Tyagi AK, Girija KG, Pillaia CGS, SharmG, Effect of doping on the morphology and multiferroic properties of $BiFeO_3$ nanorods. Nanoscale 2010; **2**, 1149-1154

[28] Gao F, Yuan Y, Wang KF, Chen XY, Chen F, Liu JM, Ren ZF, Preparation and photoabsorption characterization of $BiFeO_3$ nanowires. Appl. Phys. Lett. 2006; **89**, 102506-3

[29] Xie SH, Li JY, Proksch R, Liu YM, Zhou YC, Liu YY, Ou Y, Lan LN, Qiao Y, Nanocrystalline multiferroic $BiFeO_3$ ultrafine fibers by sol-gel based Electrospinning. Appl. Phys. Lett. 2008; **93**, 222904-3

[30] Gupta R, Chaudhary S, Kotnala RK. Interfacial Charge Induced Magnetoelectric Coupling at $BiFeO_3$/$BaTiO_3$ Bilayer Interface. *ACS Appl. Mater. Interf.* 2015; **7(16)**, 8472-8479

[31] Chaturvedi S, Das R, Poddar P, S Kulkarni. Tunable band gap and coercivity of bismuth ferrite-polyaniline core-shell nanoparticles: the role of shell thickness. RSC Adv., 2015, **5**, 23563-23568

[32] Aimon NM, Kim DH, Sun XY, Ross CA. Multiferroic Behavior of Templated $BiFeO_3$-$CoFe_2O_4$ Self-Assembled Nanocomposites. ACS Appl. Mater. Interf. 2015; **7**, 2263-2268

[33] Lorenz M, Lazenka V, Schwinkendorf P, Bern F, Ziese M, Modarresi H, Volodin A, Van Bael MJ, Temst K, Vantomme A, Grundmann M. Multiferroic $BaTiO_3$–$BiFeO_3$ composite thin films and multilayers: strain engineering and magnetoelectric coupling. J. Phys. D: Appl. Phys. 2014; **47**, 135303-10

[34] Lorenz M, Wagner G, Lazenka V, Schwinkendorf P, Modarresi H, Van Bael MJ, Vantomme A, Temst K, Oeckler O, Grundmann M. Correlation of magnetoelectric coupling in

multiferroic $BaTiO_3$-$BiFeO_3$ superlattices with oxygen vacancies and antiphase octahedral rotations. Appl. Phys. Lett. 2015; **106**, 012905

[35] Wang J, Neaton JB, Zheng H, Nagarajan V, Ogale SB, Liu B, Viehland D, Vaithyanathan V, Schlom DG, Waghmare UV, Spaldin NA, Rabe KM, Wuttig M, Ramesh R. Epitaxial $BiFeO_3$ Multiferroic Thin Film Heterostructures. Science 2003; **299**, 1719-1722

[36] Kotnala RK, Gupta R, Chaudhary S. Giant magnetoelectric coupling interaction in $BaTiO_3$/$BiFeO_3$/$BaTiO_3$ trilayer multiferroic heterostructures. Appl. Phys. Lett. 2015; **107**, 08290

[37] Kumar N, Shukla A, Kumar N, Choudhary RNP, Kumar A. Structural, electrical, and multiferroic characteristics of lead-free multiferroic: $Bi(Co_{0.5}Ti_{0.5})O_3$-$BiFeO_3$ solid solution. RSC Adv. 2018, **8**, 36939-36950

[38] Chu YH, He Q, Yang CH, Yu P, Martin LW, Shafer P, Ramesh R. Nanoscale Control of Domain Architectures in $BiFeO_3$ Thin Films. Nano Lett. 2009; 9(4), 1727-1730

[39] Park TJ, Papaefthymiou GC, Viescas AJ, Moodenbaugh AR, Wong SS. Size-dependent magnetic properties of single-crystalline multiferroic $BiFeO_3$ nanoparticles. Nano Lett. 2007; **7(3)**, 766-772

[40] Bajpai OP, Mandal S, Ananthakrishnan R, Mandal P, Khastgir D, Chattopadhyay S. Structural Features, Magnetic Properties and Photocatalytic Activity of Bismuth Ferrite Nanoparticles Grafted on Graphene Nanosheets. **New J. Chem.** 2018; **42**, 10712-10723

[41] Amrillah T, Bitla Y, Shin K, Yang T, Hsieh YH, Chiou YY, Liu HJ, Do TH, Su D, Chen YC, Jen SU, Chen LQ, Kim KH, Juang JY, Chu YH. Flexible Multiferroic Bulk Heterojunction with Giant Magnetoelectric Coupling via van der Waals Epitaxy. ACS Nano 2017; **11**, 6122-6130

[42] Catalan G, Scott JF. Physics and Applications of Bismuth Ferrite. Adv. Mater. 2009; **21**, 2463-2485

[43] Yuan X, Shi L, Zhao J, Zhou S, Miao X, Guo J. Tunability of bandgap and magnetism in K and Pb Co-doped $BiFeO_3$ nanoparticles for multiferroic applications: The Role of structural transition and Fe deficiency. *ACS Appl. Nano Mater.* 2019; **2(4)**, 1995-2004

[44] Kumar A, Kumar A, Saha S, Basumatary H, Ranjan R. Ferromagnetism in the multiferroic alloy systems $BiFeO_3$-$BaTiO_3$ and $BiFeO_3$-$SrTiO_3$: Intrinsic or extrinsic?. Appl. Phys. Lett. 2019; **114**, 022902

[45] Jian G, Xue F, Gao M, Guo Y. Orientation dependence of magnetic properties in $BiFeO_3$. J. Magn. Magn. Mater. 2019; **476**, 188-193

[46] Coey JMD, Douvalis AP, Fitzgerald CB, Venkatesan M. Ferromagnetism in Fe-doped SnO_2 thin films. Appl. Phys. Lett. 2004; **84**, 1332

[47] Neel L. Compt. Rend. 1961; **252**, 4075-4080.

[48] Neel L. In Low Temperature Physics. Eds. Gordon and Beach: London, 1962; **411**.

[49] Wu L, Dong C, Chen H, Yao J, Jiang C, Xue D, Varela JA. Hydrothermal synthesis and magnetic properties of bismuth ferrites nanocrystals with various morphology. J. Am. Ceram. Soc. 2012; **95**, 3922-3927

[50] Dutta DP, Mandal BP, Naik R, Lawes G, Tyagi AK. Magnetic, ferroelectric, and magnetocapacitive properties of sonochemically synthesized Sc-doped $BiFeO_3$

Nanoparticles. J. Phys. Chem. C 2013; **117**, 2382-2389

[51] Chen J, Tang Z, Zhao S. Giant magnetoelectric coupling effect in lead-free perovskite $BiFeO_3/Na_{0.5}Bi_{4.5}Ti_4O_{15}$ composite films. J. Alloys Compd. 2017; **712**, 256-262

[52] Pan Q, Chu B. Enhanced magnetoelectric response in bismuth-deficient $BiFeO_3$-$BaTiO_3$ ceramics. J. Appl. Phys. 2019; **125**, 154102

[53] Verma KC, Kotnala RK. Multiferroic magnetoelectric coupling and relaxor ferroelectric behavior in $0.7BiFeO_3$-$0.3BaTiO_3$ nanocrystals. Solid State Commun. 2011; **151**, 920-923

[54] Shirolkar MM, Li J, Dong X, Li M, Wang H. Controlling the ferroelectric and resistive switching properties of $BiFeO_3$ thin film prepared using sub - 5 nm dimension nanoparticles. **Phys. Chem. Chem. Phys.** 2017; **19**, 26085-26097

[55] Verma KC, Singh D, Kumar S, Kotnala RK. Multiferroic effects in $MFe_2O_4/BaTiO_3$ (M = Mn, Co, Ni, Zn) Nanocomposites. J. Alloys Compd. 2017; **709**, 344-355

[56] Verma KC, Singh M, Kotnala RK, Goyal N. Magnetic field control of polarization/capacitance/voltage/resistance through lattice strain in $BaTiO_3$-$CoFe_2O_4$ multiferroic nanocomposite. J. Magn. Magn. Mater. 2019; **469**, 483-493

[57] Pan L, Yuan Q, Liao Z, Qin L, Bi J, Gao D, Wu J, Wu H, Ye ZG. Superior room-temperature magnetic field-dependent magnetoelectric effect in $BiFeO_3$-based multiferroic. J. Alloys Compd. 2018; **762**, 184-189

[58] Jochum JK, Lorenz M, Gunnlaugsson HP, Patzig C, Hoche T, Grundmann M, Vantomme A, Temst K, Van Bael MJ, Lazenka V. Impact of magnetization and hyperfine field distribution on high magnetoelectric coupling strength in $BaTiO_3$-$BiFeO_3$ multilayers. **Nanoscale**, 2018, **10**, 5574-5580

[59] Lazenka V, Lorez M, Modarresi H, Bisht M, Ruffer R, Bonholzer M, Grundmann M, Van Bael MJ, Vantomme A, Temst K. Magnetic spin structure and magnetoelectric coupling in $BiFeO_3$-$BaTiO_3$ multilayer. Appl. Phys. Lett. 2015; **106**, 082904

[60] Verma KC, Kotnala RK. Multiferroic approach for Cr,Mn,Fe,Co, Ni,Cu substituted $BaTiO_3$ nanoparticles. Mater. Res. Exp.2016; **3**, 055006

[61] Yang B, Jin L, Wei R, Tang X, Hu L, Tong P, Yang J, Song W, Dai J, Zhu X, Sun Y, Zhang S, Wang X, Cheng Z, Chemical Solution Route for High-Quality Multiferroic $BiFeO_3$ Thin Films. Small 2019; **doi.org/10.1002/smll.201903663**, 1903663-19

[62] Sun B, Han P, Zhao W, Liu Y, Chen P, White-Light-Controlled Magnetic and Ferroelectric Properties in Multiferroic $BiFeO_3$ Square Nanosheets. J. Phys. Chem. C 2014; **118**, 18814-18819

[63] Kolte J, Daryapurkar AS, Agarwal M, Gulwade DD, Gopalan P, Magnetoelectric properties of microwave sintered $BiFeO_3$ and $Bi_{0.90}La_{0.10}Fe_{0.95}Mn_{0.05}O_3$ Nanoceramics. Mater. Chem. Phys. 2017; **193**, 253-259

[64] Rout J, Choudhary RNP, Structural transformation and multiferroic properties of Ba-Mn co-doped $BiFeO_3$. Phys. Lett. A 2016; **380**, 288-292

[65] Banerjee M, Mukherjee A, Banerjee A, Das D, Basu S, Enhancement of multiferroic properties and unusual magnetic phase transition in Eu doped bismuth ferrite nanoparticles. New J. Chem. 2017; **41**, 10985-10991

[66] Mukherjee A, Basu S, Manna PK, Yusuf SM, Pal M, Giant magnetodielectric and enhanced multiferroic properties of Sm doped bismuth ferrite nanoparticles. J. Mater. Chem. C 2014; **2**, 5885-5891

[67] Dutta DP, Mandal BP, Mukadam MD, Yusuf SM, Tyagi AK, Improved magnetic and ferroelectric properties of Sc and Ti codoped multiferroic nano $BiFeO_3$ prepared via sonochemical synthesis. Dalton Trans. 2014; **43**, 7838-7846

[68] Puli VS, Pradhan DK, Gollapudi S, Coondoo I, Panwar N, Adireddy S, Chrisey DB, Katiyar RS, Magnetoelectric coupling effect in transition metal modified polycrystalline $BiFeO_3$ thin films. J. Mag. Magn. Mater. 2014; **369**, 9-13

[69] Yang S, Ma G, Xu L, Deng C, Wang X, Improved ferroelectric properties and band-gap tuning in $BiFeO_3$ films via substitution of Mn. RSC Adv. 2019; **9**, 29238-29245

[70] Jena AK, Satapathy S, Mohanty J, Magnetic properties and oxygen migration induced resistive switching effect in Y substituted multiferroic bismuth ferrite. Phys. Chem. Chem. Phys. 2019; **21**, 15854-15860

[71] Marzouki A, Loyau V, Gemeiner P, Bessais L, Dkhil B, Megrich A, Increase of magnetic and magnetoelectric properties in Co/Mn co-doped BiFeO3 multiferroic. J. Mag. Magn. Mater. 2020; **498**, 166137

[72] Li CX, Yang B, Zhang ST, Zhang R, Sun Y, Zhang HJ, Cao WW, Enhanced Multiferroic and Magnetocapacitive Properties of (1–x) $Ba_{0.7}Ca_{0.3}TiO_3$–x$BiFeO_3$ Ceramics. J. Am. Ceram. Soc. 2014; **97 [3]**, 816-825

[73] Behera C, Choudhary RNP, Das PR, Structural, Electrical and Multiferroic Characteristics of Thermo-mechanically Fabricated $BiFeO_3$-(BaSr)TiO_3 Solid Solutions. *Mater. Res. Expr.* 2018; **5**, 056301

[74] Qi X, Zhang M, Zhang X, Gu Y, Zhu H, Yang W, Li Y, Compositional dependence of ferromagnetic and magnetoelectric effect properties in $BaTiO_3$–$BiFeO_3$–$LaFeO_3$ solid solutions. RSC Adv. 2017; **7**, 51801-51806

[75] Ummer RP, Thevenot RC, Rouxel D, Thomas S, Kalarikkal N, Electric, magnetic, piezoelectric and magnetoelectric studies of phase pure ($BiFeO_3$-$NaNbO_3$)-(P(VDF-TrFE)) nanocomposite films prepared by spin coating. RSC Adv. 2016; **6**, 28069-28080

[76] Calisir I, Amirov A A, Kleppe AK, Hall DA, Optimisation of functional properties in lead-free $BiFeO_3$-$BaTiO_3$ ceramics through La^{3+} substitution strategy. **J. Mater. Chem. A** 2018; **6**, 5378-5397

[77] Gupta R, Shah J, Chaudhary S, Singh S, Kotnala RK, Magnetoelectric coupling-induced anisotropy in multiferroic nanocomposite (1 - x) $BiFeO_3$–x$BaTiO_3$. J Nanopart Res 2013; **15**, 2004

[78] Remya KP, Rajalakshmi R, Ponpandian N, Development of $BiFeO_3$/$MnFe_2O_4$ ferrite nanocomposites with enhanced magnetic and electrical properties. Nanoscale Adv. 2020; **2**, 2968-2976

[79] Jin C, Geng W, Wang L, Han W, Zheng D, Hu S, Ye M, Xu Z, Ji Y, Zhao J, Chen Z, Wang G, Tang Y, Zhu Y, Mac X, Chen L, Tuning Ferroelectricity and Ferromagnetism in $BiFeO_3$/$BiMnO_3$ Superlattices. Nanoscale 2020; **12**, 9810-9816

[80] Sheoran N, Kumar A, Kumar V, Chahar M, Banerjee A, Structural and multiferroic properties of $BiFeO_3$/$MgLa_{0.025}Fe_{1.975}O_4$ nanocomposite synthesized by sol-gel auto combustion route. J. Mater. Sci. 2020; **31**, 2788

[81] Sufyan M, Atiq S, Abbas SK, Younis M, Riaz S, Naseem S, Magnetically driven robust polarization in (1-*x*) $BiFeO_3$-*x*$PbTiO_3$ multiferroic composites. 2019; **238**, 10-12

[82] Jain A, Wang YG, Wang N, Li Y, Wang FL, Existence of heterogeneous phases with significant improvement in electrical and magnetoelectric properties of $BaFe_{12}O_{19}$/$BiFeO_3$ multiferroic ceramic composites. Cer. Int. 2019; **45**, 22889-22898

[83] Alam M, Talukdar S, Mandal K, Multiferroic properties of bilayered $BiFeO_3$/$CoFe_2O_4$ nano-hollowspheres. Mater. Lett. 2018; **210**, 80-83

[84] Shariq M, Kaur D, Chandel VS, Jain PK, Florence S, Sharma M, Hussain S, Study of Structural, Magnetic and Optical Properties of $BiFeO_3$-$PbTiO_3$ Multiferroic Composites. Arab. J. Sci. Engg. 2019; **44**, 613-621